University of Texas Rio Grande Valley

ScholarWorks @ UTRGV

12-2020

Developing a UHF/VHF Phased-Array Satellite Ground Station

Brent K. Cole
The University of Texas Rio Grande Valley

Follow this and additional works at: https://scholarworks.utrgv.edu/etd

Part of the Physics Commons

DEVELOPING A UHF/VHF PHASED-ARRAY

SATELLITE GROUND STATION

A Thesis

by

BRENT K. COLE

Submitted to the Graduate College of
The University of Texas Rio Grande Valley
In partial fulfillment of the requirements for the degree of

MASTER OF SCIENCE

December 2020

Major Subject: Physics

DEVELOPING A UHF/VHF PHASED-ARRAY

SATELLITE GROUND STATION

A Thesis
by
BRENT K. COLE

COMMITTEE MEMBERS

Dr. Volker Quetschke
Chair of Committee

Dr. Teviet Creighton
Committee Member

Dr. Soma Mukherjee
Committee Member

December 2020

ABSTRACT

Cole, Brent K., <u>Developing a UHF/VHF Phased-Array Satellite Ground Station</u>. Master of Science (MS), December, 2020, 57 pp., 6 tables, 28 figures, 25 references.

Earth-satellite communications and tracking of spacecraft are accomplished using ground stations. Traditionally, this has been achieved by using a large parabolic antenna or pair of antennas that point at a source of interest and mechanically steer the antenna(s) as the source moves throughout the sky. Phased arrays, which have often been used in radio astronomy, can provide multiple benefits when used as a ground station including fast scanning speeds across the sky, tracking and communication of multiple sources simultaneously, and significant improvements to overall gain, signal-to-noise ratio (SNR), and data bandwidth. This thesis presents a preliminary analysis of a 20-element UHF/VHF phased array which achieves an additional 13.2dB of gain when compared to a single antenna. Additionally, a directional sensitivity of 2.2 degrees in the UHF-band and 6.2 degrees in the VHF-band has been shown. This array is intended to be located at the University of Texas Rio Grande Valley (UTRGV) Brownsville campus for the purpose of communicating with and tracking low-Earth orbit (LEO) satellites.

ACKNOWLEDGMENTS

TABLE OF CONTENTS

LIST OF TABLES

LIST OF FIGURES

CHAPTER I

INTRODUCTION

1.1 Ground Stations

An earth (or ground) station is defined by the International Telecommunications Union (ITU) as "a station located either on the Earth's surface or within the major portion of the Earth's atmosphere and intended for communication with one or more space stations" [1]. A ground station consists of at least one antenna and its associated electronics (such as amplifiers, transceivers, and computers) which serve as the telecommunication link between spacecraft and Earth.
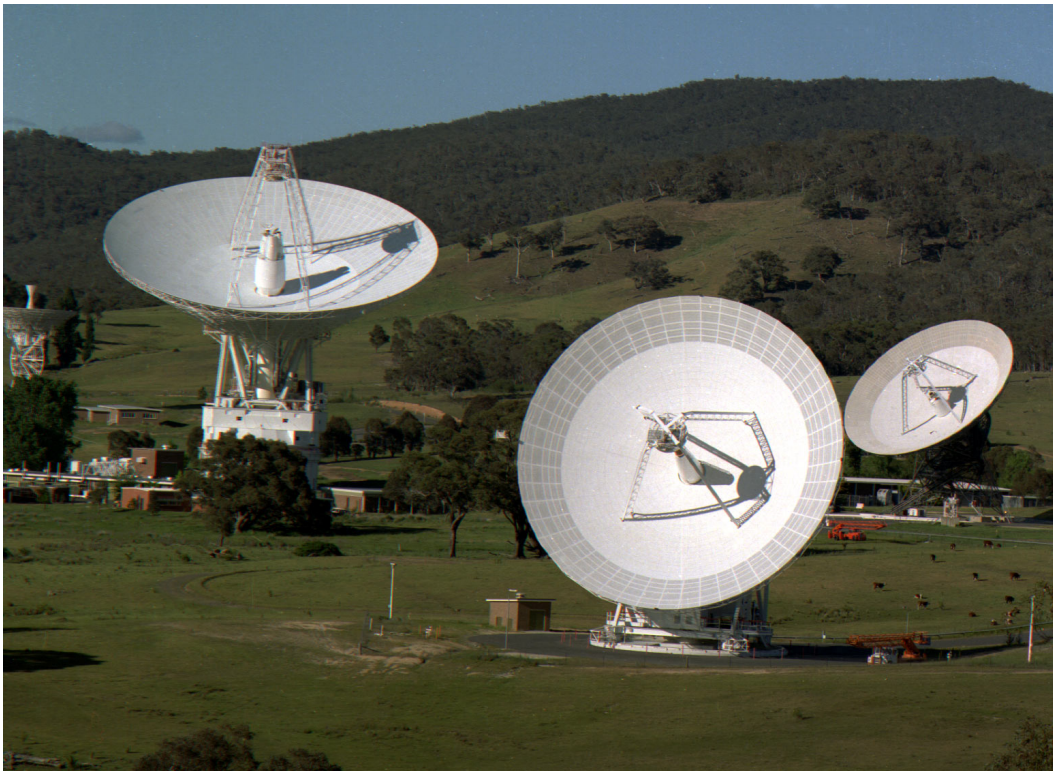
Figure 1.1: One of NASA's ground stations located in Canberra, Australia as part of the Deep Space Network (DSN) [2].

One of the first ground stations in the world was the Pleumeur-Bodou Ground Station in Northern France, whose construction was completed in 1962. It was the site where they received the first TV satellite transmission between the United States and Europe [3][4]. The satellite which facilitated this first transmission, which was manufactured by Bell Labs and launched by NASA, was Telstar 1. Although the Pleumeur-Bodou Ground Station was the first to actually receive the broadcast, which included a message from President John F. Kennedy, another ground station set to receive the same broadcast in England did not. The Goonhilly Satellite Earth Station in the UK actually suffered from a misunderstanding of the term "right-handed circular polarization" (RHCP) [5]. They were filtering out the wrong polarization, but the engineers were able to quickly adjust and receive the broadcast that same day.
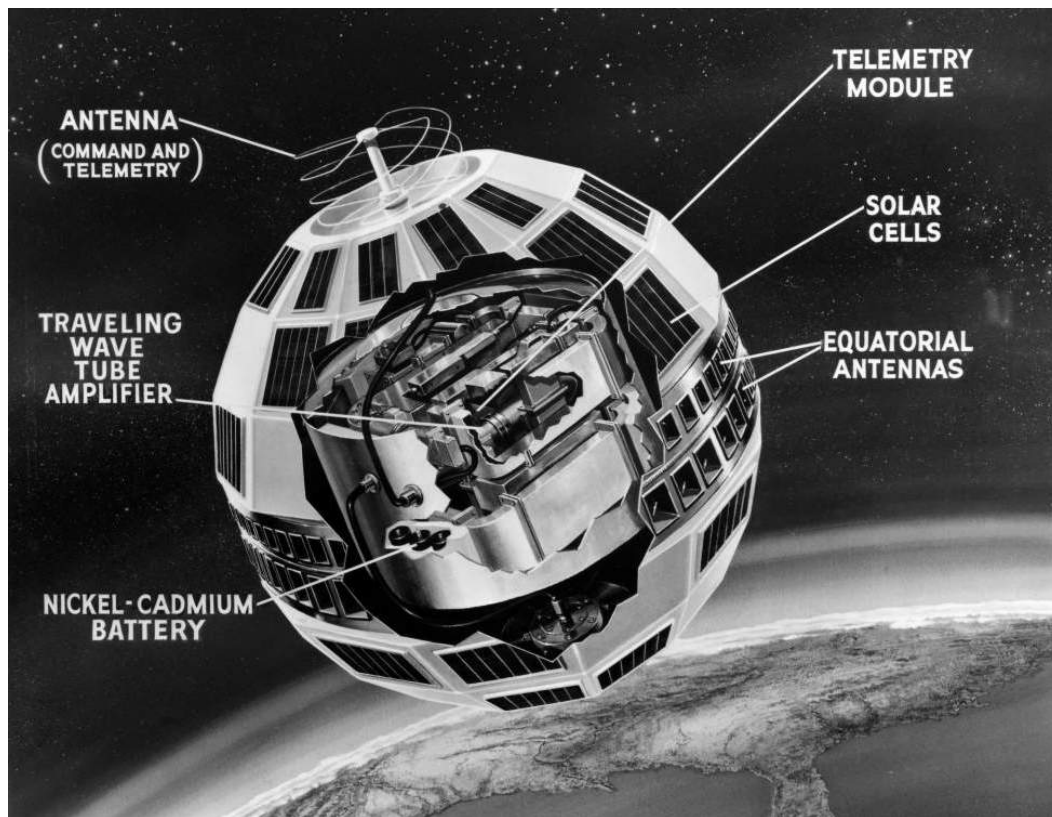
Figure 1.2: A depiction of the Telstar 1 satellite [6].

Today, ground stations play an integral part in the monitoring of space assets. As the cost per kilogram of orbital payloads and the barrier for entry into orbit continues to be driven down [7], there has been a recent increased commercial interest for ground stations and ground station networks by companies entering into the NewSpace landscape. Notable examples of this are Amazon Web Services' (AWS) Ground Station Network, ATLAS Space Operations' Freedom Network, and RBC Signals' Ground Station Network.

1.2 Phased Arrays

Traditionally, major ground stations around the world have used large parabolic dish antennas (see, for example, figure 1.1). There are limitations to using just a single parabolic antenna for receiving and/or transmitting such as the need to mechanically steer the antenna to track the source of interest, only being able to track and/or communicate with one source at a time, and slow scanning speeds across the sky. One alternative to this is to use a phased array.

A phased array is an array of antennas in which the phase of each individual antenna can be varied such that the overall beam produced as a result of the array can be shaped and directed without the need to physically move any of the antennas [8]. The first phased array was demonstrated in 1905 by Karl Ferdinand Braun, who would later go on to win the Nobel Prize in Physics in 1909 for his work with Guglielmo Marconi in developing wireless telegraphy [9]. Braun's first phased array consisted of 3 monopole antennas arranged in an equilateral triangle in which he could insert a quarter-wave delay in the feedline of any single antenna, effectively allowing for him to rotate the beam of the array by $120°$.

Phased arrays can provide many benefits over a single dish including increasing overall gain, improved signal-to-noise ratio (SNR), direction of arrival (DOA) estimation, electronic beam steering, significantly faster scanning speeds, no mechanically moving parts, increased data bandwidth, and simultaneous tracking and communication with several satellites.

Today, phased arrays are widely used in AM/FM broadcasts to enhance signal strength and coverage area, in radar to detect and simultaneously track multiple ships, aircraft, or projectiles, and more recently in 5G communication systems to enable massive multiple-input, multiple-output (MIMO) performance and achieve significantly faster data rates[10][11].

Figure 1.3: The Precision Acquisition Vehicle Entry Phased Array Warning System (PAVE PAWS) at Clear Air Force Base in Alaska was built for the U.S. Air Force in the 1970s with a total of 2,677 crossed-dipole elements in two circular arrays.

1.3 Phased Array Ground Stations

Ground stations have largely employed the use of large parabolic antennas because of their high gain and directivity, however, the difficulty associated with keeping the narrow beam on-source and maintenance of the high wind-load structures can be considerably cost-intensive [12]. With the increasing prevalence of low-cost antennas and radio-frequency electronics such as transceivers, phased arrays are now considered as a cost-effective alternative to parabolic dish antennas with

notable commercial examples currently undergoing testing and development such as ATLAS Space Operations' LINKS Electronically Steered Array and Lockheed Martin's Verge ground station [13][14].

The ground station proposed in this thesis is a 20-element, multi-band phased array arranged in a psuedorandom arrangement and is made up of 20 UHF crossed-yagi antennas operating at 435MHz in the 70cm band and 20 VHF crossed-yagi antennas operating at 145MHz in the 2m band, common operating bands for LEO satellites. A pseudorandom arrangement was chosen to maximize sidelobe suppression. What follows in this thesis is a description of antenna and antenna array fundamentals, a description of the hardware selected, and a computational model with an analysis that compares a pseudorandom arrangement, a uniform arrangement, and a single antenna consistent with the hardware selected.

CHAPTER II

THEORY

2.1 Electromagnetic Waves

Electromagnetic waves are self-propagating oscillations in electric and magnetic fields and their behavior is dictated by Maxwell's equations shown below in SI units:

$$\nabla \cdot \mathbf{E} = \frac{\rho}{\varepsilon_0} \qquad\qquad \nabla \times \mathbf{E} = -\frac{\partial \mathbf{B}}{\partial t}$$

$$\nabla \cdot \mathbf{B} = 0 \qquad\qquad \nabla \times \mathbf{B} = \mu_0 \left(\mathbf{J} + \varepsilon_0 \frac{\partial \mathbf{E}}{\partial t} \right)$$

By manipulating Maxwell's equations in free space (i.e., $\rho = \mathbf{J} = 0$), one can arrive at the following wave equations for the electric field, $\mathbf{E}$, and magnetic field, $\mathbf{B}$, respectively:

$$\frac{1}{c^2} \frac{\partial^2 \mathbf{E}}{\partial t^2} - \nabla^2 \mathbf{E} = 0$$
$$\frac{1}{c^2} \frac{\partial^2 \mathbf{B}}{\partial t^2} - \nabla^2 \mathbf{B} = 0. \tag{2.1}$$

These are second-order partial differential equations whose solutions describe the propagation of electromagnetic waves in a vacuum and are collectively known as the electromagnetic wave equations. One set of plane wave solutions to these equations is

$$\mathbf{E}(\mathbf{r},t) = \Re\{\mathbf{E}(\mathbf{r})e^{i\omega t}\} = \mathbf{E}_0 \cos\left(\omega t - \mathbf{k} \cdot \mathbf{r} + \varphi\right)$$
$$\mathbf{B}(\mathbf{r},t) = \Re\{\mathbf{B}(\mathbf{r})e^{i\omega t}\} = \mathbf{B}_0 \cos\left(\omega t - \mathbf{k} \cdot \mathbf{r} + \varphi\right) \tag{2.2}$$

where i is the imaginary unit, $\omega = 2\pi f$ is the angular frequency, f is the frequency, t is time, $\mathbf{E}_0$ is the amplitude of the electric field, $\mathbf{B}_0$ is the amplitude of the magnetic field, $\mathbf{k} = (k_x, k_y, k_z)$ is the

wave vector and points in the direction of propagation, k is the wavenumber, $\mathbf{r}$ is the position vector, and φ is a phase angle. The wave number, k, is defined by

$$k = |\mathbf{k}| = \frac{2\pi}{\lambda}. \tag{2.3}$$

where λ is the wavelength.

From the first of Maxwell's equations and the equation describing the electric field in equation 2.2, one can see that

$$\nabla \cdot \mathbf{E} = 0 \implies$$

$$\nabla \cdot \mathbf{E}_0 \cos(\omega t - \mathbf{k} \cdot \mathbf{r} + \varphi) = 0 \implies$$

$$\mathbf{k} \cdot \mathbf{E}_0 \sin(\omega t - \mathbf{k} \cdot \mathbf{r} + \varphi) = 0$$

which can only be true for all t and r if the electric field is orthogonal to the direction of the wave propagation (i.e., $\mathbf{k} \cdot \mathbf{E}_0 = 0$). Similarly for the magnetic field,

$$\nabla \cdot \mathbf{B} = 0 \implies$$

$$\nabla \cdot \mathbf{B}_0 \cos(\omega t - \mathbf{k} \cdot \mathbf{r} + \varphi) = 0 \implies$$

$$\mathbf{k} \cdot \mathbf{B}_0 \sin(\omega t - \mathbf{k} \cdot \mathbf{r} + \varphi) = 0$$

which shows that the magnetic field is also orthogonal to the direction of wave propagation (i.e., $\mathbf{k} \cdot \mathbf{B}_0 = 0$). Additionally, from looking at another one of Maxwell's equations:

$$\nabla \times \mathbf{B} = \mu_0 \varepsilon_0 \frac{\partial \mathbf{E}}{\partial t} \tag{2.4}$$

one can see that, since $\frac{\partial \mathbf{E}}{\partial t}$ points in the same direction as $\mathbf{E}$, and $\nabla \times \mathbf{B}$ is perpendicular to $\mathbf{B}$, then as a consequence $\mathbf{E}$ must be perpendicular to $\mathbf{B}$.

In short, electromagnetic waves travelling in free space can be described as *transverse* waves whose electric and magnetic fields are orthogonal to one another and orthogonal to the direction of

7

propagation.

A characteristic property of electromagnetic radiation is its "polarization". By convention, an electromagnetic wave's polarization refers to the direction of the electric field oscillation. For instance, for a wave traveling in the $+z$ direction, the electric field can oscillate in any direction that lies in the *x-y* plane. We say that an electromagnetic wave is linearly polarized in the *x*-direction if the associated electric field is

$$\mathbf{E} = E_0 \cos(\omega t - \mathbf{k} \cdot \mathbf{r} + \varphi)\hat{\mathbf{x}}. \tag{2.5}$$

In general, we say a wave is linearly polarized if the electric field vector oscillates only in a single direction. A wave's polarization is sometimes referred to as "vertical" or "horizontal" if the electric field vector only oscillates up and down or left and right, respectively.
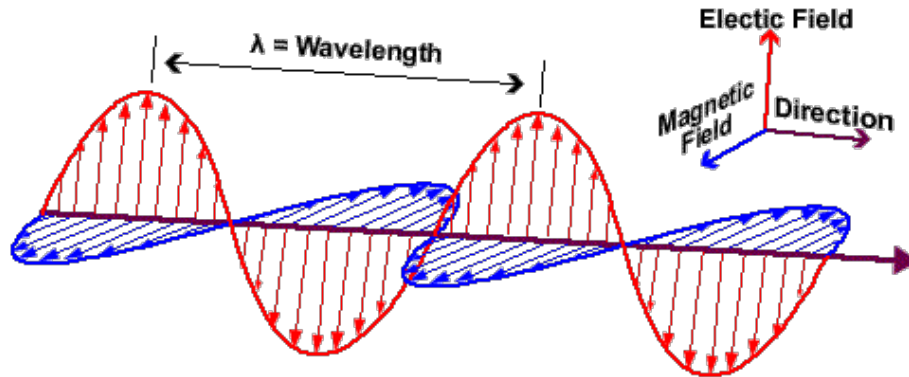
Figure 2.1: A depiction of a linearly polarized electromagnetic wave whose electric field, magnetic field, and direction of propagation are all shown to be orthogonal to one another.

Additionally, another type of polarization of interest is circular polarization, wherein the electric field has a constant magnitude, but whose direction rotates at a constant rate in a plane perpendicular to the direction of the wave propagation. Mathematically, this can be described as the sum of two linear polarized waves out of phase by $\frac{\pi}{2}$.

For example,

$$\mathbf{E} = E_0\cos(\omega t - k_z z)\hat{\mathbf{x}} - E_0\sin(\omega t - k_z z)\hat{\mathbf{y}} \qquad (2.6)$$

describes an electromagnetic wave propagating in the $+z$ direction in which the y-component of the electric field leads the x-component by $\frac{\pi}{2}$.

Circular polarization also has a property known as "handedness" which refers to the direction of the electric field's rotation. From the point of view of a source generating an electromagnetic wave, we say that the wave is right-handed circularly polarized if one points their right thumb in the direction of propagation and the other fingers curl in the direction of the electric field's temporal rotation at a point in space. Likewise, from the point of a source, a wave is said to be left-handed circularly polarized if one points their left thumb in the direction of propagation and the other fingers curl in the direction of the electric field's temporal rotation. These two handedness conventions are depicted in Figure 2.2.
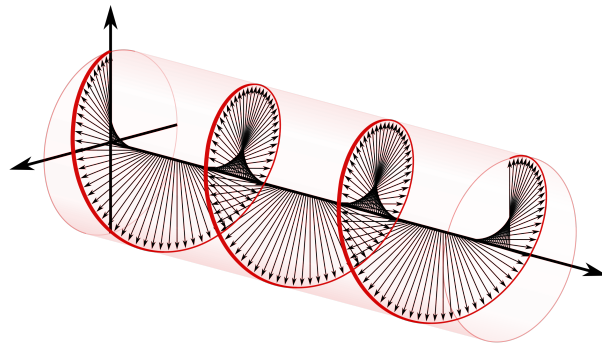
(a) A right handed circularly polarized wave.
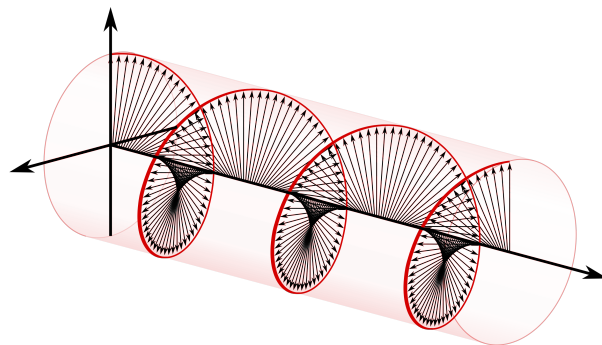
(b) A left handed circularly polarized wave.

Figure 2.2: A depiction of right-handed and left-handed circularly polarized waves.

It is important to note that the definitions stated above are from the point of view of a source. If one defines right-handedness and left-handedness from the point of view of a receiver, then one points their thumb *away* from the direction of propagation and matches the remaining fingers to the direction of the electric field's temporal rotation. Though different conventions are used in different fields of study, in the context of engineering and radio astronomy, the convention of characterizing the electric field's rotation from the point of view of the source is a general rule [15][16]. This has led to a significant source of confusion and explains the aforementioned incident with Goonhilly initially failing to receive the first satellite TV transmission.

2.2 Fundamental Antenna Theory

Antennas are the tools with which radio waves can either be received or transmitted. In reception, an incoming electromagnetic wave will impart a voltage on conductive elements of the antenna and an electric current can be measured at the antenna terminals. In transmission, an electric current supplied at the antenna terminals generate radiating electromagnetic waves.

Let P_o be the total power radiated by an antenna and $U_\mathrm{rad}(\theta, \varphi)$ be the radiant intensity expressed in units of W and W/sr, respectively. Here, θ describes the zenith angle while φ describes the azimuth angle in a spherical coordinate system (ISO 80000-2:2019 convention). Then, the total radiated power can be found by integrating the radiant intensity over the surface of a sphere:

$$P_\mathrm{o} = \int_0^{2\pi} \int_0^{\pi} U_\mathrm{rad}(\theta, \varphi) \sin\theta \, d\theta \, d\varphi. \tag{2.7}$$

The directivity, $D(\theta, \varphi)$, is a unitless measure of an antenna's capability to concentrate radiated power in a particular direction and is defined as the ratio of the radiant intensity that that antenna creates in a particular direction to the average value over all directions (i.e., to an isotropic antenna):

$$D(\theta, \varphi) = \frac{U_\mathrm{rad}(\theta, \varphi)}{P_\mathrm{o}/(4\pi)} \tag{2.8}$$
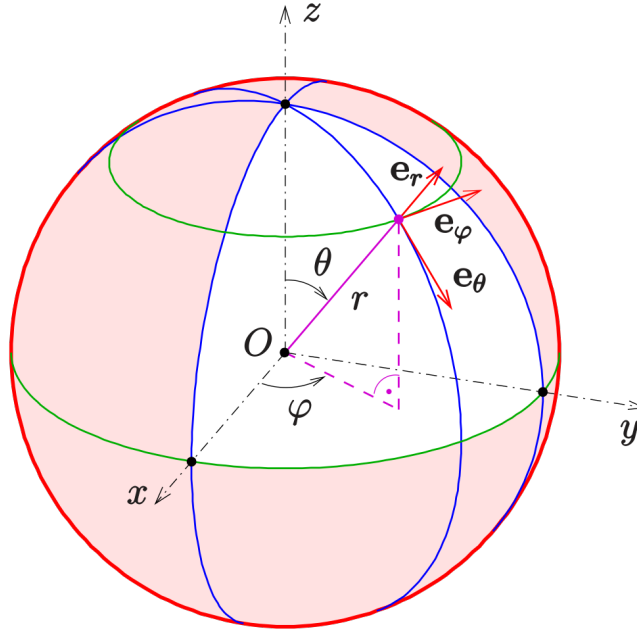
Figure 2.3: The spherical coordinate system as defined by the ISO 80000-2:2019 convention and commonly used in physics.

Let P_{in} be the power accepted by an antenna at the feedpoint in units of W. Then, the radiation efficiency of an antenna is defined to be:

$$\varepsilon_{\text{ant}} = \frac{P_{\text{o}}}{P_{\text{in}}}. \tag{2.9}$$

The gain of an antenna in a given direction takes into account the antenna's efficiency and its directivity in that direction. That is,

$$G(\theta, \varphi) = \varepsilon_{\text{ant}} D(\theta, \varphi) \tag{2.10}$$

which is also unitless. As can be seen from equation 2.10, in a perfectly efficient (or lossless) antenna (i.e., $\varepsilon_{\text{ant}} = 1$), the gain and the directivity are identical. Whenever the gain, $G(\theta, \varphi)$, or directivity, $D(\theta, \varphi)$, of an antenna are stated without reference to a particular direction it is understood that they refer to the maximum value of the respective parameter and can be written in a

shorter form and independently of θ or φ as just G or D. Most often, the directivity and gain are are expressed in units of decibels (dB). For completeness, those expressions are shown below:

$$G_{\mathrm{dBi}} = 10\log_{10}(G) \tag{2.11}$$

where the letter "i" in dBi is used in reference to the fact that the gain and directivity, as can be seen from equations 2.8 and 2.10, are defined with respect to an isotropically radiating antenna. Likewise,

$$D_{\mathrm{dBi}} = 10\log_{10}(D). \tag{2.12}$$

The effective area, or effective aperture, of an antenna, A_{eff}, is defined as the area, oriented perpendicular to the direction of an incoming electromagnetic wave, which would intercept the same amount of power from that wave as the antenna receiving it and is related to its gain by the following equation:

$$A_{\mathrm{eff}}(\theta, \varphi) = \frac{\lambda^2}{4\pi} G(\theta, \varphi) \tag{2.13}$$

where λ is the wavelength in units of meters and A_{eff} is in units of m^2. The received power, P_r, of an incident wave with power density E_t, where E_t is defined as

$$E_t = \frac{P_t}{4\pi r^2} G_t \tag{2.14}$$

in units of W/m^2, is related to the receiving antenna's effective aperture, $A_{\mathrm{eff,r}}$, by the following equation:

$$P_r = E_t \cdot A_{\mathrm{eff,r}}. \tag{2.15}$$

Substituting in the definition of the power density and effective aperture yields

$$P_r = \left(\frac{P_t}{4\pi r^2} G_t\right) \left(\frac{\lambda^2}{4\pi} G_r\right)$$

or equivalently,

$$P_r = \left(\frac{\lambda}{4\pi r}\right)^2 G_t G_r P_t \tag{2.16}$$

which is also known as the Friis transmission equation.

Gain, directivity, field strength, and other quantities that have an angular dependence and which are related to the antenna's sensitivity to received or transmitted electromagnetic waves can be visualized with a far-field radiation pattern, denoted as $\bar{f}(\theta, \varphi)$. Far-field, in this context, refers to the region in which the electric and magnetic fields fall off as $\sim 1/R$ and are dominated by radiative fields. This is contrasted by the near-field which is dominated by reactive fields which fall off as $\sim 1/R^2$ and $\sim 1/R^3$. The distance, d_F, that defines the limit between far-field and near-field is given [17] by:

$$d_F = \frac{2D^2}{\lambda} \tag{2.17}$$

where D is the largest dimension of the antenna. This is also known as the Fraunhofer distance.
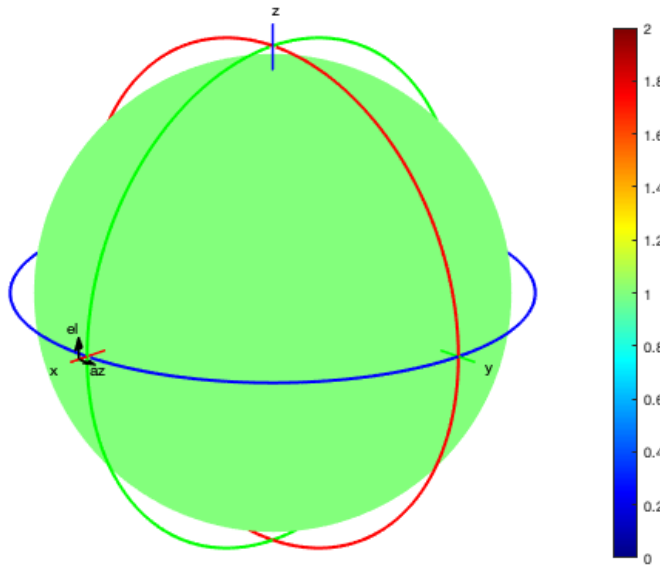
Figure 2.4: A 3D representation of the far-field radiation pattern for a single isotropic antenna. Here, color represents magnitude of the electric field. As expected, the radiation pattern shows equal intensity in all directions and is visualized as a sphere.

Additionally, the electromagnetic reciprocity theorem states that the electrical properties of a lossless antenna such as its gain, directivity, and efficiency are the same whether the antenna is used for either reception or transmission. So an antenna's transmitting characteristics can be immediately known from its receiving characteristics and vice versa.

Another important property of antennas is its beamwidth, also called the half-power beamwidth (HPBW), is the angle span between the half-power points with respect to the antenna's main lobe. The main lobe is defined is the lobe where the maximum of the antennas radiation pattern is present. This can be visualized by taking a slice of a 3D patterns in either an azimuthal or zenith angle and plotting them in a polar form. An example of such a slice is shown in Figure 2.5 below.
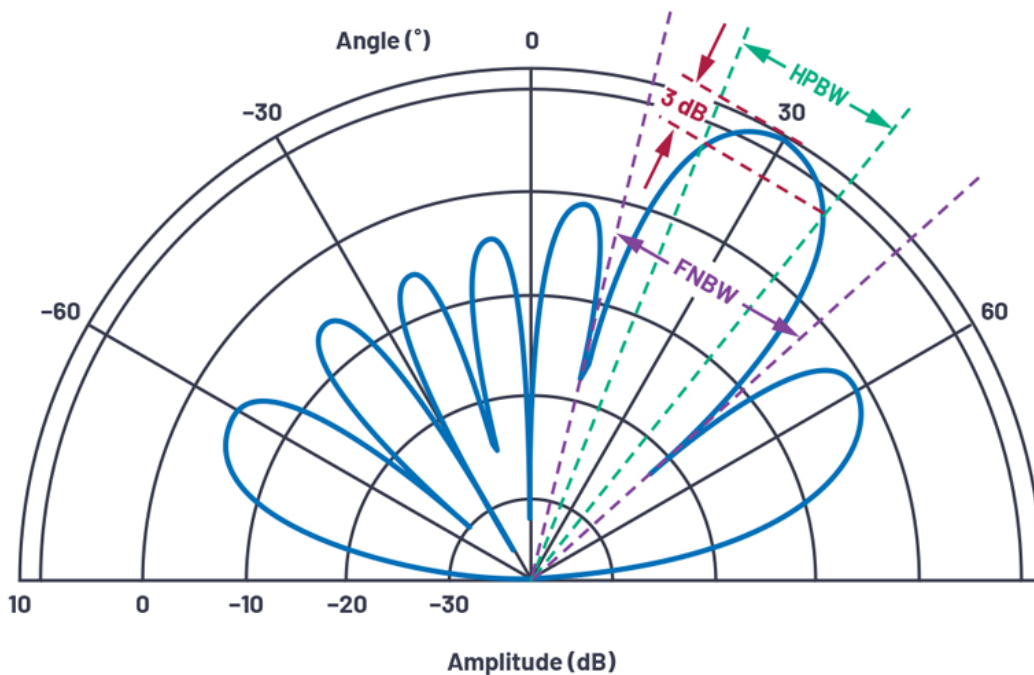
Figure 2.5: A 2D representation of a beam pattern along elevation angles (from $-90°$ to $+90°$). Note that this is a polar plot where the radial tick marks measure amplitude in dB and the main lobe is the largest amplitude lobe. The HPBW is shown as the angle span which indicates a -3dB drop from the maximum amplitude. Also shown is the first null beam width (FNBW) [18].

14

2.3 Fundamental Antenna Array Theory

If all the antenna elements in an antenna array are identical and have the same physical orientation, then the radiation pattern for an antenna array, $\bar{Y}(\theta, \varphi)$ is simply the array factor multiplied by the individual element's radiation pattern, $\bar{f}(\theta, \varphi)$. That is,

$$\bar{Y}(\theta, \varphi) = \bar{f}(\theta, \varphi) \cdot AF(\theta, \varphi) \tag{2.18}$$

where $AF(\theta, \varphi)$ is the array factor. Generally, the array factor is defined as:

$$AF(\theta, \varphi) = \sum_{m=1}^{N} I_m e^{-i(k\hat{\mathbf{r}} \cdot \mathbf{r}'_m)} \tag{2.19}$$

where I_m is the complex amplitude of the excitation of the mth element, i is the imaginary unit, k is the wave number, $\hat{\mathbf{r}}$ is the unit position vector pointing in the direction of interest, and $\mathbf{r}'_m$ is the position vector of the mth element. As can be seen from equation 2.19, the array factor depends on the positions of all the antenna elements as well as the excitation at each element.

The overall array radiant intensity, directivity, and gain are proportional to the radiant intensity, directivity, and gain of a single element. Explicitly, they are related by:

$$\begin{aligned} U_{\text{array}} &= |AF(\theta, \varphi)|^2 \cdot U(\theta, \varphi) \\ D_{\text{array}} &= |AF(\theta, \varphi)|^2 \cdot D(\theta, \varphi) \\ G_{\text{array}} &= |AF(\theta, \varphi)|^2 \cdot G(\theta, \varphi) \end{aligned} \tag{2.20}$$

The angular resolution of an antenna array, R, is defined as

$$R = \frac{\lambda}{B} \tag{2.21}$$

where B is the largest physical separation of the antennas in the array. If a source is smaller than the angular resolution it is called a point source, otherwise, it's called a diffuse source.

CHAPTER III

SYSTEM ARCHITECTURE

The antennas to be used for this ground station are M2 Antenna's 436CP16 and 2MCP8A antennas operating at 435MHz and 145MHz, respectively. These are right-handed circularly polarized (RHCP) crossed-yagi antennas optimized for LEO satellite communications and were selected to minimize attenuation due to polarization mismatch. It is common for satellites to use circularly polarized antennas since the orientation of the antenna can change depending on the satellite's attitude throughout its orbit.

Transmit Antenna Polarization	Receive Antenna Polarization	Theoretical Loss (dB)
Vertical	Vertical	0
Vertical	Horizontal	$-\infty$
Vertical	(RH or LH) Circular	-3
Horizontal	Vertical	$-\infty$
Horizontal	Horizontal	0
Horizontal	(RH or LH) Circular	-3
RH Circular	RH Circular	0
RH Circular	LH Circular	$-\infty$

Table 3.1: Theoretical loss expressed in decibels (dB) for different transmit and receiving antenna polarizations.

The antennas are rear-mounted on a 9-foot cross-boom included with M2 Antenna's LEO-pack. The cross-boom is installed on an AlfaSpid BIG RAS rotator which means that each of the independent elements is capable of being mechanically steered. The rotator is then mounted on a 10-foot long, 2-inch outer-diameter (OD) rigid conduit which acts as the antenna mast. The bottom of the mast is machined in-house for the addition of torsion bars and is cemented in a 5-gallon bucket of concrete. For added mechanical stability, four 1/4" eyebolts are added to the mast which

serve as mounting points for guying the antenna mast. Each eyebolt on the antenna mast is then guyed to another eyebolt which has been cemented in another 5-gallon bucket of concrete including torsion rods. A proof-of-concept prototype was built and is shown assembled in the STARGATE lab in Figure 3.1 (note: antennas shown are different than the aforementioned 436CP16 and 2MCP8A).

Figure 3.1: Showing a pair of antennas attached to a cross-boom, mounted on a BigRAS rotator, cemented in a concrete bucket, the supporting guy wire, and respective mounting points.

After the antenna assembly is complete, the 5 buckets are buried into the Earth as can be seen in Figure 3.2. Twenty of these such antenna assemblies with one UHF antenna and one VHF antenna per assembly will be installed in a large open field located at UTRGV's Brownsville campus.

Figure 3.2: A completed antenna assembly installed outside the UTRGV STARGATE facility.

With this proof-of-concept prototype, we were able to successfully demonstrate that data could be downlinked from a satellite. Shown in Figure 3.3 is the result of a 137MHz signal transmitted from the NOAA 19 satellite. This signal is an automatic picture transmission (APT) which consists of a 256-level amplitude modulated 2400Hz subcarrier, which is then frequency modulated onto the 137 MHz-band RF carrier. After being demodulated, the signal is decoded using software such as WXtoImg to produce the two images seen, which are taken at different wavelengths.
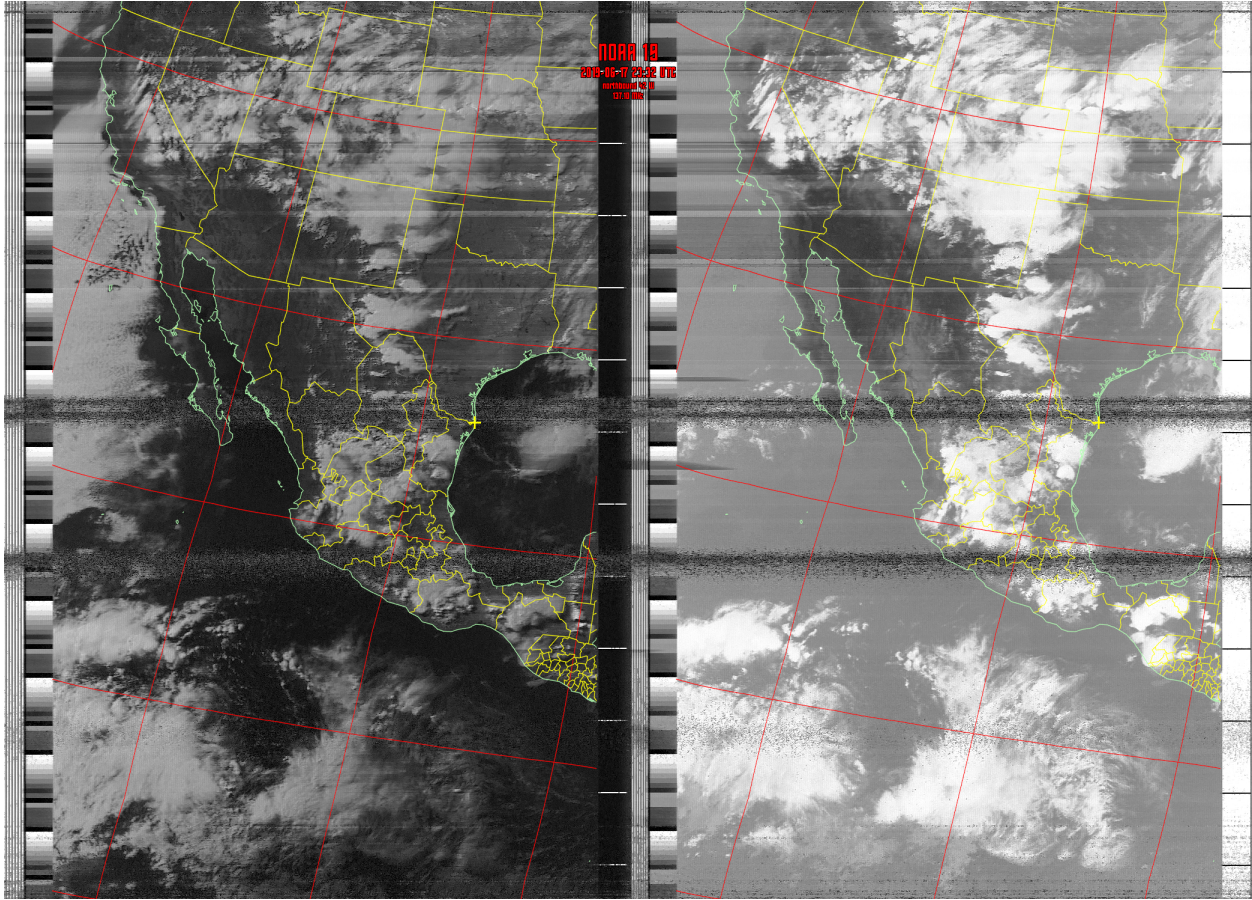
Figure 3.3: Satellite imagery data downlinked from NOAA 19 using the STARGATE proof-of-concept ground station.

3.1 Receiving Signal Chain

The analog receiving signal chain is similar for both UHF and VHF segments. Beginning at the antenna, the signal enters a mast-mounted preamplifier which serves to overcome resistive losses in the coaxial cable runs, minimize noise introduced into the system, and amplify the signal of interest. The pre-amplifiers are gallium arsenide field-effect transistor (GaAsFET) devices that are equipped with automatic RF switching which disengage the pre-amplifier whenever the antenna is to be used for transmission. GaAsFET devices are known for their sensitivity and low noise profiles, which make them optimal components for weak signals such as those used in radio astronomy and space communications.

Pre-Amplifier Characteristics		
	VHF	UHF
Model:	KP-2-2M	KP-2-440
Frequency Range (MHz):	144-148	430-450
Gain (dB):	10-15/15-20	10-15/15-20
NF (dB):	0.6	0.6
Operating Voltage (V):	13.6 - 15	13.6 - 15
P_{max} (W):	100	100

Table 3.2: Characteristics for the pre-amplifiers chosen for the UHF and VHF bands. Both pre-amplifiers allow for a LOW or HIGH gain setting, which is why the gain is displayed as two ranges.

Next, the signal passes through an ATT3G50MHP DC-passing surge protector which serves to protect the electronics inside the control room from being damaged by lightning. In the event that lightning strikes, the surge protector shorts the discharge to ground, so care should be taken to properly ground each surge protector. These were chosen to be DC-passing so that the required 15VDC to power the pre-amplifiers from the control room could pass through unimpeded. Additionally, the surge protectors have a gas tube backup, 2000W of power handling capability, and a typical loss of 0.1dB at 1GHz with excellent broadband performance.

Then, the signal passes through approximately 250 feet of low-loss LMR-400 coaxial cable. The attenuation in dB/100ft in LMR-400 cable is given by the datasheet [19]:

$$\text{Attenuation (dB/100ft)} = (0.122290)\sqrt{f_{\text{MHz}}} + (0.000260) \cdot f_{\text{MHz}}. \tag{3.1}$$

The attenuation at 145MHz and 435MHz for LMR-400 are 1.51dB/100ft and 2.66dB/100ft, respectively. This means that for a 250-foot cable run, the total attenuation will be 3.78dB and 6.65dB for the VHF and UHF bands, respectively.

Lastly, the signal enters the ICOM IC-9700 receiver where the RF signal is directly sampled

in both the UHF and VHF bands. This is in contrast to the heterodyning RF architecture. In a heterodyning system, the received signal is downconverted to a lower, intermediate frequency (IF) through use of a local oscillator (LO) and then filtered, amplified, demodulated, and then digitized.

In a direct sampling RF architecture, the system simply consists of a low-noise amplifier (LNA), an appropriate filter, and an analog-to-digital converter (ADC). Because there are less analog components, direct sampling has a smaller form factor and is more power efficient. The added components in a heterodyning system introduce unwanted sources of noise in the signal chain and have limitations associated with the non-linear nature of mixers. It is beneficial to use direct sampling in phased-array systems where achieving phase coherence between large numbers of antennas requires the synchronization of LOs in addition to the synchronization of clocks across devices. Because there are no LOs in a direct-sampling architecture, there is no requirement for LO synchronization which can significantly simplify designs [20].
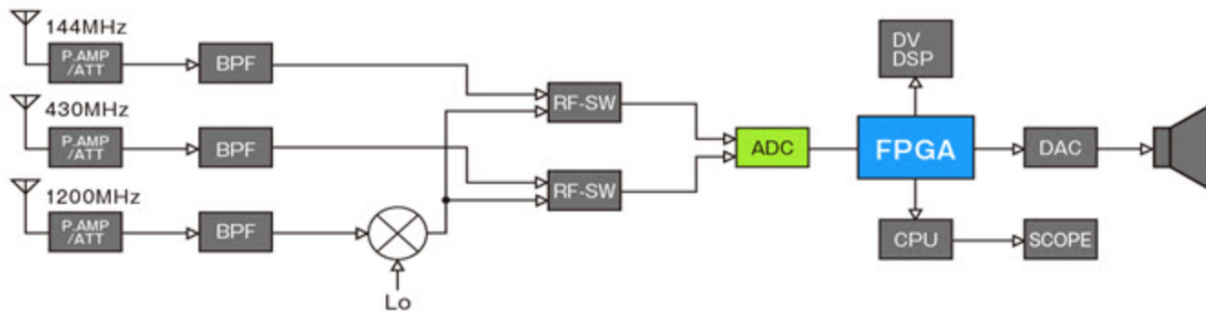
Figure 3.4: Block diagram for Icom IC-9700 receiver.

In addition to the 144MHz and 430MHz bands, the IC-9700 also operates at 1200MHz, however this utilizes an LO to downconvert the signal to a 60MHz bandwidth between 311MHz and 371MHz. The IC-9700 transceiver employs an LTC2156-14 dual-channel, 14-bit, 210MHz (max) sampling ADC in which the dual-channels enable receiving on two channels simultaneously.

In digital signal processing, a fundamental theorem known as the Nyquist-Shannon sampling theorem places a restriction on the minimum sample rate with which to capture all the information from a continuous-time signal using a discrete set of samples. Stated simply, the restriction is that the sampling frequency, f_s, should be at least twice the highest frequency, f_H, contained in the

signal of interest or information about that signal will be lost [21].

Explicitly, this restriction, known as the Nyquist criterion, can be stated as:

$$f_s > 2f_H. \tag{3.2}$$

For a signal that is sampled at less than $2f_H$, aliasing will occur. Aliasing is a phenomena in which different signals become indistinguishable from one another when sampled, the result of which can be seen in Figure 3.5.
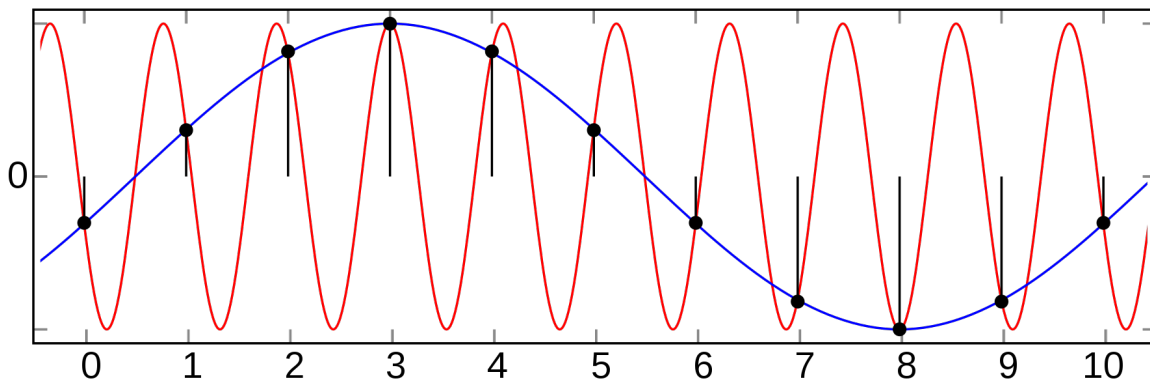
Figure 3.5: An example of aliasing. Multiple sinusoids of different frequencies can be constructed to represent the same set of discrete points.

Though aliasing is typically unwanted and regarded as a source of distortion in many fields, it can actually be a useful tool in sampling *bandpass* signals, or signals that have no low-frequency content, which can be accomplished through the use of the appropriate "anti-alias" bandpass filters. The process of intentionally sampling at a rate lower than $2f_H$ is known as undersampling and can effectively convert bandpass signals to baseband signals. In fact, the Nyquist criterion can be restated as: the sampling frequency f_s need only be at least twice the *bandwidth*, B, of the signal of interest or information about that signal will be lost. In other words,

$$f_s > 2B. \tag{3.3}$$

The distinction between equation 3.3 and equation 3.2 is important because equation 3.3 makes no reference to the absolute frequencies contained within the signal, only its bandwidth. For instance, in order to sample FM radio signals in the frequency range from 88-108MHz (a 20MHz bandwidth), one does not need to sample at least 216MHz, only at least 40MHz. The IC-9700 makes use of this and is able to sample signals in the 1240 - 1300MHz range by sampling at a rate greater than twice the bandwidth (where $f_{s,\max} = 196.6\text{MHz} > 2B = 120\text{MHz}$).

After the signal has been digitized by the ADC, the data is processed in the digital domain using an on-board field-programmable gate array (FPGA) and an ARM processor.

3.2 Transmitting Signal Chain

The transmitting segment begins at the IC-9700 with the FPGA processing any input provided either through a microphone or computer and feeds a digital bit stream to a digital-to-analog converter (DAC). The IC-9700 employs a 16-bit dual-channel DAC sampled at 1179MHz. For the 70cm and 2m band signals, these signals are amplified with an internal power amplifier (PA), pass through a low-pass filter, and exit the appropriate ports on the transceiver. The 23cm band signal is generated as a 311-371MHz IF source before it is upconverted using a mixer and LO, passed through a basspass filter, amplified with an internal power amplifier, a low pass filter, and finally exits the appropriate port on the transceiver. As can be seen in Table 3.3, depending on the transmitting modulation mode, the output power from the IC-9700 varies.
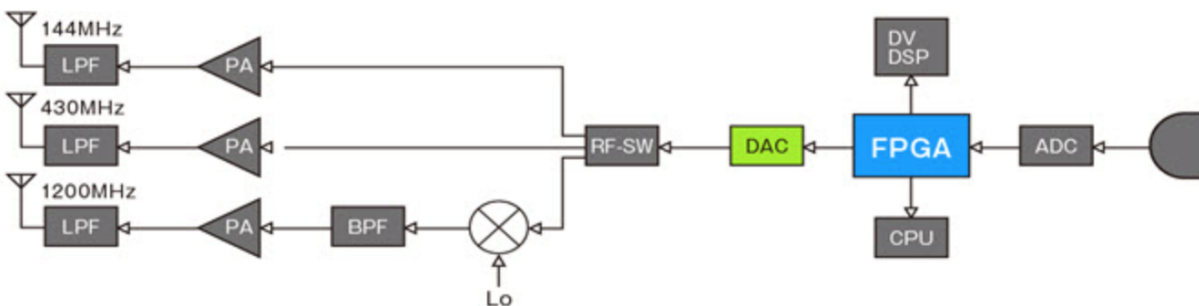
Figure 3.6: Block diagram for Icom IC-9700 transmitter.

	Output Power (W)	
Frequency Band (MHz)	SSB/CW/FM/RTTY/DV/DD	AM
144	0.5 - 100	0.125 - 25
430/440	0.5 - 75	0.125 - 18.75
1200	0.1 - 10	0.025 - 2.5

IC-9700 Transmitter Characteristics

Table 3.3: Output power for different modulation modes of the IC-9700 transmitter.

After exiting the IC-9700, the signal passes through the same 250-foot long run of coaxial cable with the same associated losses as given by Equation 3.1. Then, the signal passes through a DC-passing surge protector followed by the receiving preamplifier which simply acts as a through connection whenever the cable is used in transmission mode. Lastly, the signal enters the antenna where it is radiated away.

It is important to characterize the gains and the losses associated with the signal as it propagates from its source to its destination to ensure that information can intelligibly be received with an adequate signal-to-noise ratio (SNR). This type of characterization is known as a link budget analysis and will be calculated using the hardware chosen in the following section.

CHAPTER IV

LINK BUDGET ANALYSIS

A link budget analysis is an accounting of all the power gains and losses associated with a telecommunication link. A link budget can have the form of the following equation:

$$P_{RX} = P_{TX} + G_{TX} - L_{TX} - L_{FS} - L_M + G_{RX} - L_{RX} \tag{4.1}$$

where P_{RX} is the received power, P_{TX} is the transmitter output power, G_{TX} is the gain of the transmitting antenna, L_{TX} is the loss associated with the transmitter, L_{FS} is the free-space path loss, L_M is miscellaneous losses, G_{RX} is the gain of the receiving antenna, and L_{RX} is the loss associated with the receiver.

For this analysis, five candidate target satellites were chosen as initial target sources. Those sources are the International Space Station (ISS), Nihon University's SPROUT cubesat, Belarusian State University's CubeBel-1, German Orbital System's D-Star One iSat, and the Federal University of Santa Catarina's (UFSC) FloripaSat-1. A link budget analysis can be done for both the uplink (transmitting to satellite) and downlink (transmitting to ground segment). The analysis presented here will be a downlink budget for receiving UHF data packets from the ISS using a single UHF antenna.

4.1 ISS UHF Downlink

4.1.1 Transmitting segment

According to the Amateur Radio on the International Space Station (ARISS) organization, the ISS utilizes a Kenwood TM-D700 radio that supports FM and packet operations in both the 70cm and 2m band with up to 25W of power [22]. We will focus on the 70cm, or 440MHz, band. In this case, the transmitting antenna is a 6dB yagi (i.e., $G_{TX} = 6$dB) pointed nadir (directly downwards). We will assume the output power to be 25W, or, utilizing $P_{\text{dBm}} = 10\log_{10}\left(\frac{P_{\text{mW}}}{1\text{mW}}\right)$, 43.98dBm (i.e., $P_{TX} = 43.98$dBm). The output of the transmitter is connected to 10 feet of TCOM-400 coaxial cable and a bulkhead connector. Utilizing the data sheet for TCOM-400, we can approximate the transmitter losses, L_{TX}, to approximately be 0.74dB (0.15dB per connector and 0.29 for the cable alone) for the 10-foot run of cable (i.e., $L_{TX} = 0.74$ dB).

4.1.2 Free-space segment

To calculate the free-space path loss, we have to calculate the distance between the ground segment and the satellite in question. In Figure 4.1, there are a 3 distances: r_e, the radius of the Earth, d, the distance between the ground segment and the satellite, and z, the satellite's orbit radius. There are also four angles present in the figure: θ, the angle subtended by the ground segment and the satellite from the center of the Earth, ψ, the angle subtended by the center of the Earth and the satellite from the ground segment, φ, the angle subtended by the satellite and the local horizon from the ground segment, and, finally, α, the angle subtended by the center of the Earth and the ground segment from the satellite.

We'd like to determine d. Let's assume that our minimum observation elevation is $15°$. The reason that we choose the *minimum* observation angle is because that is where the free-space losses will be maximized and that is the worst-case scenario. So we set $\varphi = 15°$. Utilizing the law of sines, we can see from figure 4.1 that:

$$\frac{\sin \psi}{z} = \frac{\sin \alpha}{r_e}.$$
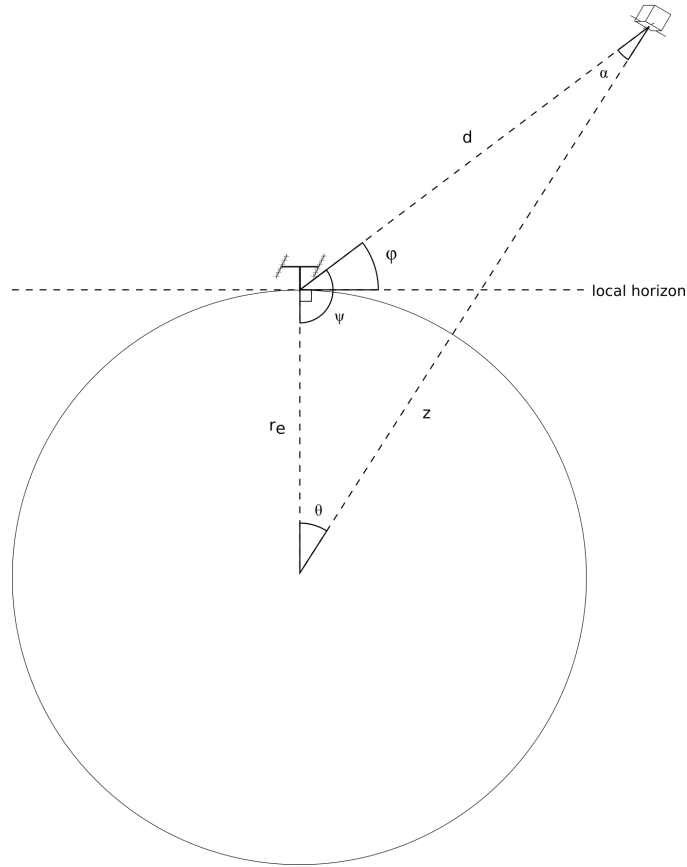
Figure 4.1: Illustration of a communication link between a ground station and a satellite.

Therefore,

$$\alpha = \sin^{-1}\left(\frac{r_e}{z}\sin\psi\right). \tag{4.2}$$

We know the radius of the Earth: $r_e = 6,378$km. z is just equal to r_e plus the average orbit altitude of the ISS, which turns out the be about 400km. Therefore, $z = 400\text{km} + 6,378\text{km} = 6,778\text{km}$. From figure 4.1, we can see that ψ is equal to the minimum elevation angle plus $90°$. Therefore, $\psi = \varphi + 90° = 105°$. Plugging these values into equation 4.2, we see that:

$$\alpha = \sin^{-1}\left[\left(\frac{6,378\text{km}}{6,778\text{km}}\right)\sin 105°\right]$$

$$= \sin^{-1}(0.9089)$$

$$= 65.36°.$$

Now that we know α and ψ, we can determine θ:

$$\theta = 180° - \alpha - \psi$$

$$= 180° - 65.36° - 105°$$

$$= 9.64°.$$

Utilizing the law of sines again, we can see from figure 4.1 that:

$$\frac{\sin \theta}{d} = \frac{\sin \psi}{z}.$$

Therefore,

$$d = \left(\frac{\sin \theta}{\sin \psi}\right) z. \tag{4.3}$$

Plugging in the values we have calculated for θ, ψ, and z into equation 4.3, we see that:

$$d = \left[\frac{\sin(9.64°)}{\sin(105°)}\right] 6,778\text{km}$$

$$= 1,175.06\text{km}.$$

To calculate the free-space path loss, we start with the Friis transmission formula:

$$\frac{P_r}{P_t} = D_t D_r \left(\frac{\lambda}{4\pi d}\right)^2 \tag{4.4}$$

where P_r is the power received, P_t is the power transmitted, D_t is the directivity of the transmitting antenna, D_r is the directivity of the receiving antenna, λ is the signal wavelength, and d is the distance between the two antennas. For simplification, we will assume that the directivities of both antennas are 1 (i.e., $D_r = D_t = 1$). This is an oversimplification, but should provide a good approximate result.

The free-space path loss (FSPL) is defined as the ratio of the power transmitted to the power received. That is,

$$\text{FSPL} = \frac{P_t}{P_r} = \left(\frac{4\pi d}{\lambda}\right)^2 = \left(\frac{4\pi df}{c}\right)^2.$$

Expressed in decibels, the free-space path loss is:

$$\text{FSPL}_{\text{(dB)}} = 10\log_{10}\left[\left(\frac{4\pi df}{c}\right)^2\right]$$
$$= 20\log_{10}\left(\frac{4\pi df}{c}\right).$$

ARISS specifies the UHF packet downlink at 437.550MHz, so we set $f = 437.550$MHz. It follows, then, that at a minimum elevation angle of $15°$, and at a frequency of 437.550MHz, we see that the free-space path loss is:

$$\text{FSPL}_{\text{(dB)}} = 20\log_{10}\left[\frac{4\pi(1,175.06\text{km})(437.550\text{MHz})}{299,792 \text{ km/s}}\right]$$
$$= 146.67\text{dB}.$$

4.1.3 Receiving segment

The receiving antenna in use for the UHF array is M2 Antenna System's 436CP16. This antenna is a circularly polarized yagi antenna with a gain of 13.3dBic. We utilize Mirage's KP-2-440 mast-mounted preamplifier, which has a maximum gain of 20dB with a noise factor (NF) of 0.6dB. The antenna is connected to approximately 200 feet of LMR-400 coaxial cable. Utilizing Equation 3.1, we can approximate the cable loss to be about 6.65dB for the UHF band.

4.1.4 Bringing it together

If we sum the values we have so far into equation 4.1, we see that we have:

$$P_{RX} = 43.98\text{dBm} + 6\text{dB} - 0.74\text{dB} - 146.67\text{dB} + 13.3\text{dB} - 6.65\text{dB} + 20\text{dB}$$
$$= -70.78\text{dBm}.$$

Under the receiver characteristics of the ICOM IC-9700 transceiver, it lists the sensitivity for FM, with a 12dB signal-to-noise and distortion ratio (SINAD), as "less than 0.18μV." We can convert this to a power, utilizing the fact that the impedance at the port is 50Ω:

$$\text{Sensitivity}_{\text{Watts}} = \frac{V^2}{R} \implies$$
$$= \frac{(0.18\mu\text{V})^2}{50\Omega}$$
$$= 6.48 \times 10^{-16} \text{ W.}$$

$$\text{Sensitivity}_{\text{dBm}} = 10\log_{10}\left(\frac{6.48 \times 10^{-16} \text{ W}}{1\text{mW}}\right)$$
$$= -121.88\text{dBm.}$$

Based on the -121.88dBm sensitivity of the receiver and the received power of -70.78dBm for receiving UHF data packets from the ISS, this indicates that the link margin is 51.1dB. In other words, the communication link can tolerate an addition 51.1dB of attenuation before the receiver can no longer intelligibly resolve UHF data packets from the ISS.

CHAPTER V

SIMULATIONAL DATA

5.1 Modeling A Yagi Antenna

In order to create an approximate model to analyze the response of the array, a simulation was created in MATLAB which modeled the individual antenna elements as well as the array itself. First, the individual elements were modeled by calling the `quadCustom` function which creates a custom Yagi antenna. This function allows the user to specify the length and spacing of the driven element, reflector, and various director elements in addition to the boom. By taking the mechanical dimensions specified in M2 Antenna's datasheets for the 436CP16 and 2MCP8A antennas and feeding them into the `quadCustom` function, we are able to first create an approximate model of the individual elements.

(a) 436CP16

(b) 2MCP8A
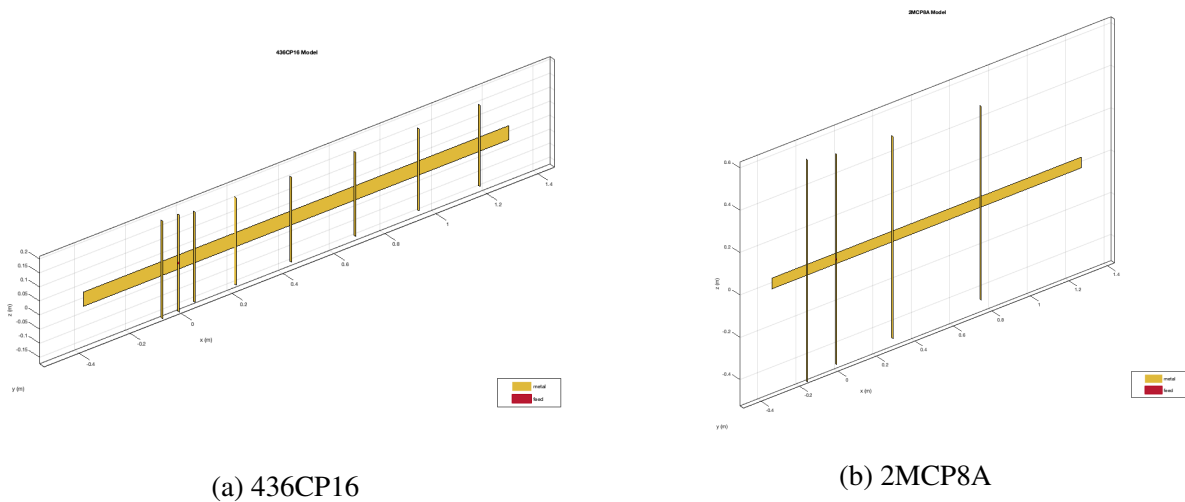
Figure 5.1: The UHF (a) and VHF (b) Yagi antennas modeled in MATLAB.

It should be noted that circular polarization is realized with these Yagi antennas by feeding the two sets of orthogonal dipoles with a quarter-wavelength phase delay between each other. However, because these two sets of dipoles are orthogonal to each other, the electric field from one set of dipoles will be independent of the other's electric field and it is sufficient when analyzing the far-field pattern to model just a single set of dipoles and not a full crossed-dipole Yagi. An example of the modeled antennas can be seen in Figure 5.1 and Figure 5.2.

(a) UHF Antenna Radiation Pattern   (b) VHF Antenna Radiation Pattern
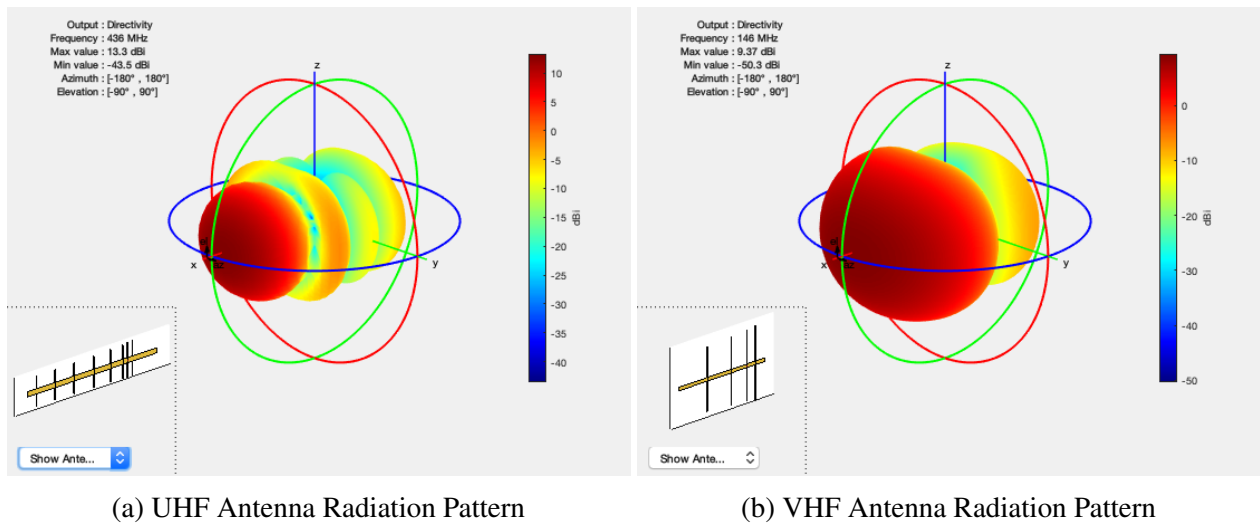
Figure 5.2: The UHF (a) and VHF (b) Yagi antennas beam patterns modeled in MATLAB.

To determine whether the model is sufficient to approximate the antenna, important antenna metrics such as the gain, front-to-back (F/B) ratio, and beamwidth were calculated at the center design frequency using the model and compared to the values stated in the datasheets. From looking at Table 5.1, it can be seen that the gain and F/B ratio are matched fairly well to the datasheet with the largest difference being 1.6dB. The modeled beamwidth has a more significant difference as compared to the datasheets and is indicative of the fact that there is more information that can be gleaned from looking at the antenna beam patterns.

	436CP16			2MCP8A		
	Datasheet	Model	Difference	Datasheet	Model	Difference
Gain (dBi):	13.3	13.3	0.0	9.2	9.37	0.17
F/B (dB):	15	16.6	1.6	16	16.4	0.4
Beamwidth (rad):	0.73	0.84	0.11	1.05	1.01	0.04

Table 5.1: The gain, front-to-back ratio (F/B), and beamwidth of the models compared to known values of the antennas.

Looking at the polar plots comparing a slice of the simulated beam pattern to that of the manufacturer's data sheet in Figure 5.3, there are a few key features to notice. For one, it should be noted that the radial axes scale differently which will obviously affect the representation of the beam pattern. Instead, we can compare particular values across the plots.

Comparing the two UHF directivity plots at the top of Figure 5.3, the first sidelobes have magnitudes approximately 15dB down from the main lobe in both plots. The angles at which these occur are $60°$ in the simulated pattern and approximately $55°$ in the datasheet. The backlobe is slightly larger in magnitude for the simulated antenna at 16.6dB down from the main lobe compared to the datasheet where it's approximately 25dB down from the main lobe.

Comparing the two VHF directivity plots at the bottom of Figure 5.3, the magnitude of the backlobes is just over -20dB in both plots with the magnitude being slightly larger in the simulated antenna compared to the datasheet. The nulls in the radiation pattern occur at $90°$ and $270°$ in the simulated antenna compared to approximately $240°$ and $120°$.

It should be noted that, at no point in creating the simulated antennas, was frequency used as a design parameter. The only parameters used in modeling the antenna were purely physical dimensions associated with the antenna elements. That the simulated response closely resembles that of the datasheet is a good indicator and, for the purposes of creating an approximate antenna model to analyze the response of the array, should serve to be sufficient.
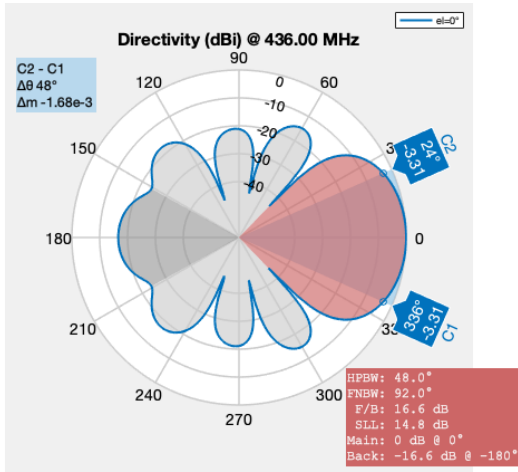
(a) UHF azimuthal pattern
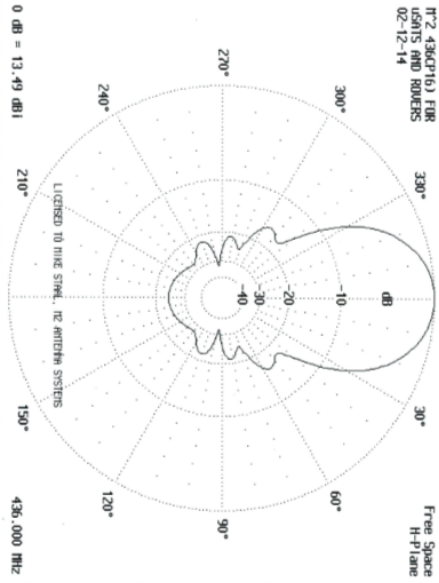
(b) UHF datasheet
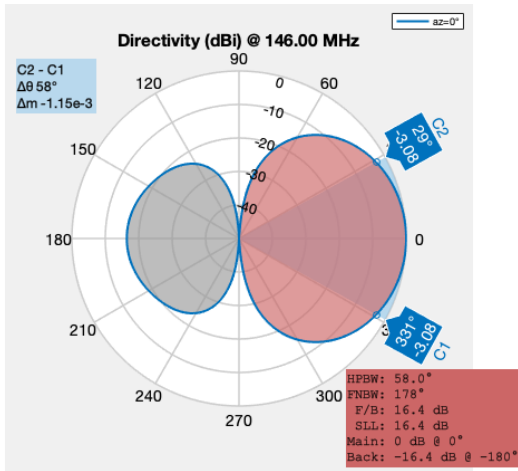
(c) VHF azimuthal pattern
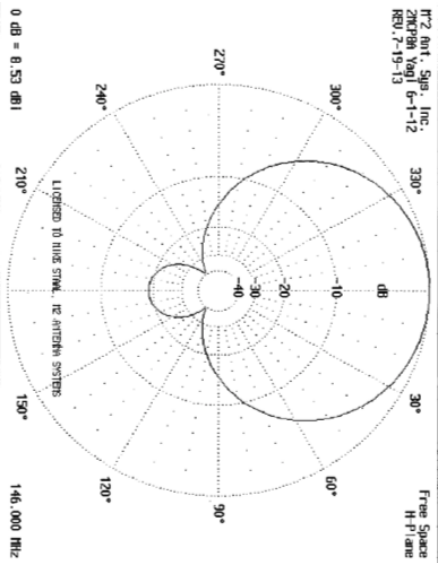
(d) VHF datasheet

Figure 5.3: The azimuthal patterns of both UHF and VHF antennas.

5.2 Array Geometry and Configuration

In general, if the spacing between elements for an array is increased, the resulting beamwidth of the radiation pattern decreases. However, increasing the size of the array introduces undesired grating lobes (or sidelobes which have amplitudes that are comparable to the main lobe). For uniformly spaced arrays, the maximum spacing between elements to avoid grating lobes is half a wavelength. Due to mechanical considerations, the elements in this array have been arranged such that each element maintains its ability to be mechanically steered and the spacing between elements is on the order of several wavelengths.

The mathematics describing grating lobes is the same as that used to describe scattering in a crystal lattice as described by Bragg's law. For instance, consider a monochromatic plane wave which is incident on a uniformly spaced array with some element separation, d, as depicted in Figure 5.4. As can be deduced from the figure, the difference in path length for a ray hitting one element will be different from an adjacent element by $d\sin(\theta)$.
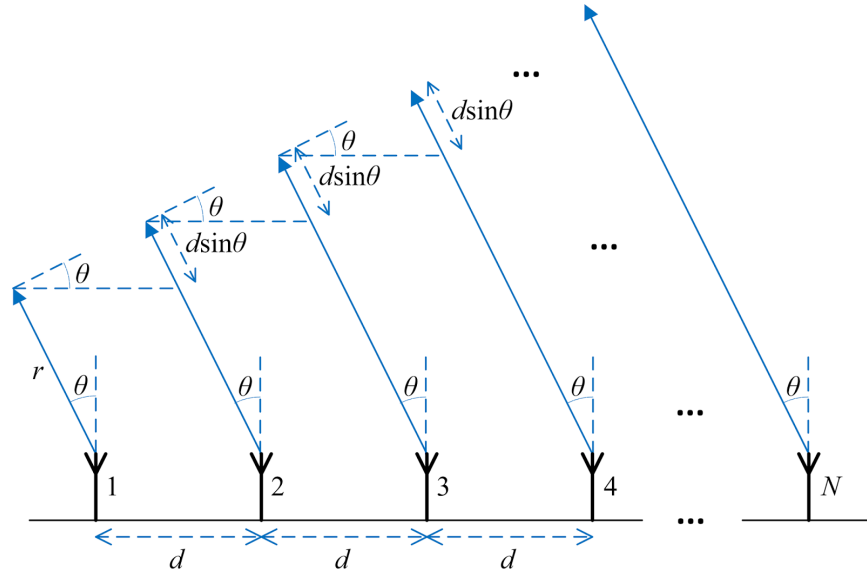
Figure 5.4: A uniformly spaced array showing a geometric delay in the arrival of an incident wavefront due to a path length difference of $d\sin(\theta)$ [23].

The condition that constructive interference occurs is when the difference in path length is equal to an integer multiple of the wavelength (i.e., $d \sin(\theta) = n\lambda$ where n is a positive integer). These points of constructive interference are realized as side lobes in phased arrays and are generally undesirable. The first point at which the waves completely and destructively interfere occurs when the difference in path length is equal to a half wavelength (i.e., $d \sin(\theta) = \frac{\lambda}{2}$). These points of destructive interference are realized as nulls. Because the domain of θ is restricted by $0 \leq \theta \leq \frac{\pi}{2}$, $\sin(\theta)$ is restricted to $0 \leq \sin(\theta) \leq 1$. Therefore, for any $d \leq \frac{\lambda}{2}$, sidelobes will not be present. Equivalently, any element spacing, d, greater than $\frac{\lambda}{2}$ will exhibit side lobes. For a uniformly spaced array, this effect will be magnified across all the elements in the array, creating sidelobe levels which are comparable to that of the main lobe. One approach to minimize side lobe levels is to use a pseudorandom array geometry. By using a pseudorandom arrangement, the number of antenna pairs for which the difference in path length for a monochromatic wavefront incident upon the array at a particular angle is equal to precisely an integer multiple of the wavelength is minimized. One tradeoff is that this comes at the cost of of a lower maximal directivity compared to a uniform arrangement.

A program was written in Python to generate pseudorandom arrangements with particular restrictions or boundary conditions. The program makes use of the `Numpy` package and the pseudocode is as follows: First, specify the number of elements in the array to be generated, a minimum radius for each element to be separated by, and an upper and lower bound for the dimensions of the rectangular array in meters. Then, the program will generate two random numbers (i.e., an (x,y) coordinate pair) from a uniformly distributed list whose bounds are given by the numbers specified in the first step. Add this coordinate to a list and generate a new coordinate. Check the newly generated coordinate with the existing coordinates in the list. If the newly generated coordinate has a Euclidean distance greater than the specified minimum radius, add it to the list. If it doesn't, generate a new random coordinate and repeat until the number of coordinates in the list reaches the number of specified elements. Using this program, whose code is shown in Appendix A, antenna element coordinates were generated and fed into MATLAB to simulate an array pattern.
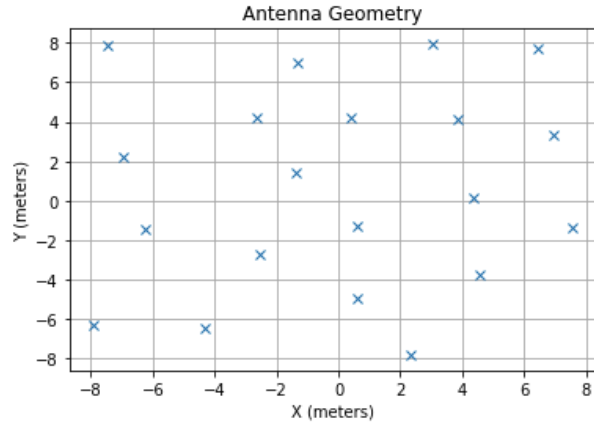
Figure 5.5: Output of the Python program which generates the antenna coordinates for a pseudorandom arrangement.

An example that will be analyzed for the remainder of this paper will be the geometry shown in Figure 5.5. This geometry was generated by requiring 20 elements with a minimum radius of 3 meters between elements and a lower and upper bound of -8 and 8 meters, respectively. In other words, it is a set of 20 (x, y) pairs such that the Euclidean distance between any two pairs is greater than or equal to 3 meters and with a restricted domain of $(x, y) \in [-8, 8)$ meters. Once generated, this set of coordinates is then fed into MATLAB where the aforementioned simulated antennas are simulated as an array. Shown in Figure 5.6 is a view of the array as modeled in MATLAB.

(a) Isometric view

(b) Top-down view
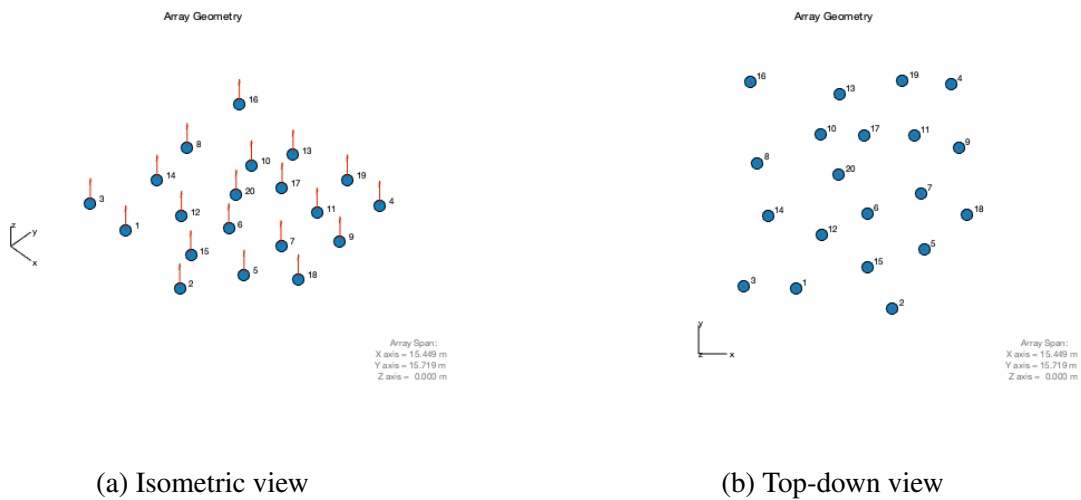
Figure 5.6: Output of MATLAB being supplied the coordinates to generate and simulate the array. Also shown are the element normals, shown pointing zenith and indicated by red arrows.

The values used to generate this geometry were chosen to allow for each "node" in the array to maintain mechanical steerability. The cross-boom, which will have a UHF and VHF antenna mounted on each end, is approximately 9-feet in length. Therefore, the closest distance that any two nodes should be separated by is 9 feet and so a minimum distance of 3 meters (equivalent to 9.84 feet) was chosen. As a result of these constraints, the resulting array response is not optimal for the frequency bands of interest. Specifically, this will be a sparsely-filled array where the sidelobes are closer to the main lobe as a result of the larger inter-element spacing, but suppressed in amplitude as a result of the pseudorandom arrangement. The area where the array will be deployed will have much more than 16 meters of space available, so any additional elements that would be added to the array would be used to expand the baseline of the array, creating a narrower pencil-beam on the sky rather than creating a densely packed array.

5.3 Array Simulations

The directivity pattern for the UHF segment of the array is shown in Figure 5.7a. Likewise, an elevation cut of the directivity pattern for the UHF segment is shown in Figure 5.7b.
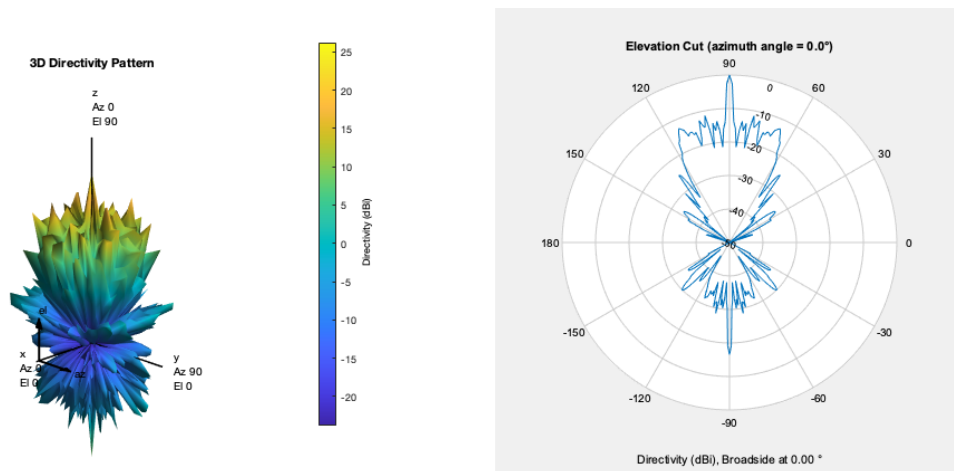
(a) Simulated 3D directivity pattern

(b) An elevation cut of the normalized directivity

Figure 5.7: The pseudorandom array response for the UHF segment.

For the UHF segment, this simulation shows that, using a pseudorandom arrangement, a main lobe directivity of 26.49dB can be achieved with a beamwidth of 2.2°. The largest sidelobe occurs at 10.9° off the main lobe at a level of 11.4dB down from the main lobe. Additionally, the

38

backlobe has a directivity of magnitude 16.5dB down from the main lobe. Also shown is the array directivity pattern using the VHF antennas in Figure 5.8a and Figure 5.8b. For the VHF segment, this simulation shows that, using a pseudorandom arrangement, a main lobe directivity of 22.61dB can be achieved with a beamwidth of 6.2°. The largest sidelobe occurs at 17.3° off the main lobe at a level of 13.9dB down from from the main lobe. Additionally, the backlobe has a directivity of magnitude of 16.4dB down from the main lobe.

(a) Simulated 3D directivity pattern   (b) An elevation cut of the normalized directivity

Figure 5.8: The pseudorandom array response for the VHF segment.

To summarize, those values are shown in Table 5.2 below. It is useful to compare the array characteristics of the pseudorandom arrangement to that of a single antenna as well as that of a uniformly spaced arrangement where the element spacing is 3m in a 5×4 geometry to show the advantages of using an array, in general, and a pseudorandom array, in particular.

	UHF	VHF
Main Lobe Level (dB):	26.49	22.61
Side Lobe Suppression (dB):	11.43	13.9
Back Lobe Level (dB):	9.97	6.22
HPBW (rad):	0.04	0.11

Table 5.2: The main lobe, side lobe, backlobe, and HPBW of the pseudorandom array.
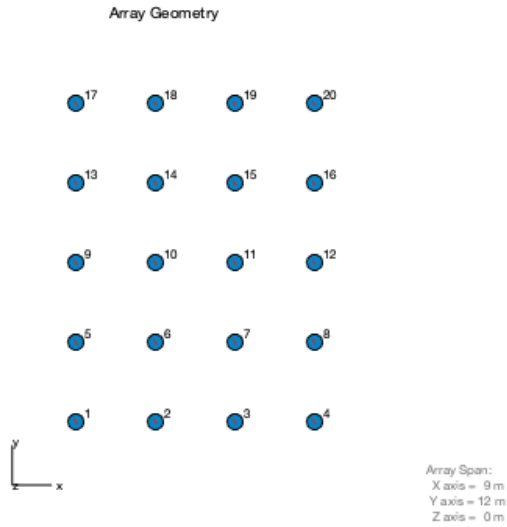
Figure 5.9: A 5×4 uniformly-spaced arrangement with an element spacing of 3 meters.

As can be seen from both the 3D directivity pattern in Figure 5.10a and the normalized directivity pattern in 5.10b for the UHF segment of a uniformly spaced array, the side lobes are clearly distinct and at a comparable level to that of the main lobe.
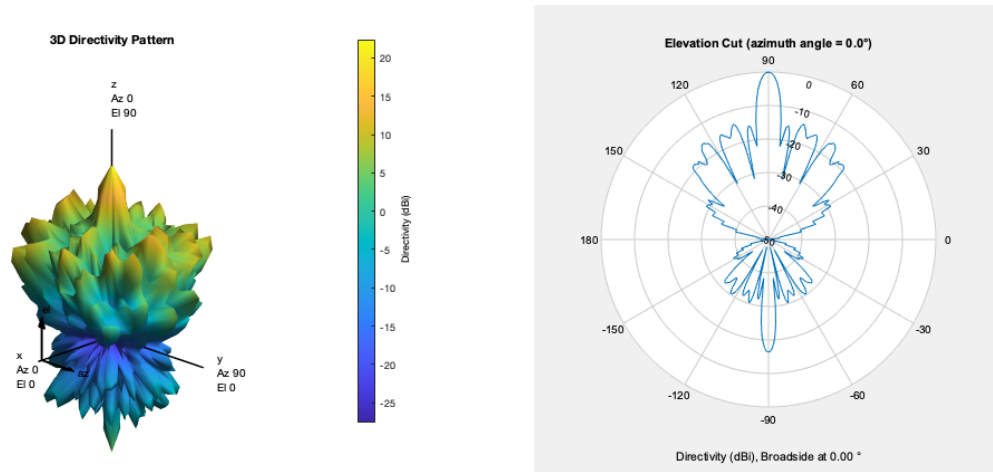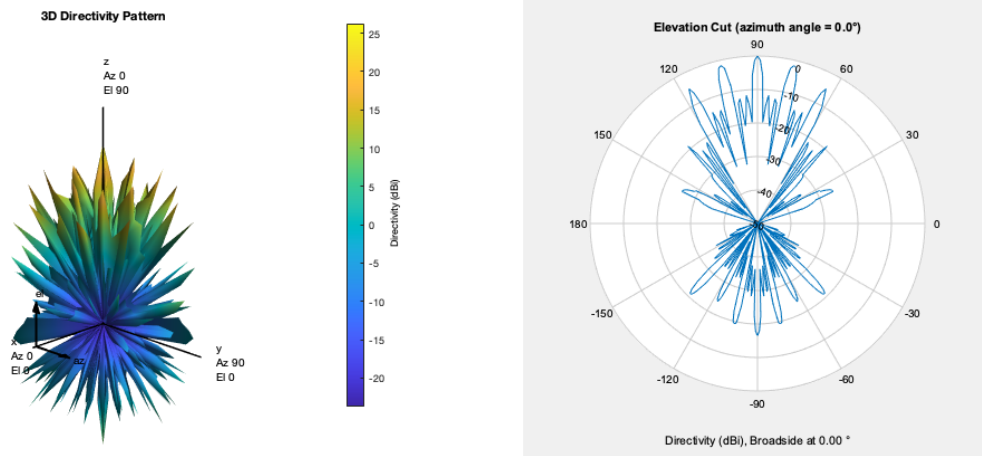

(a) Simulated 3D directivity pattern

(b) An elevation cut of the normalized directivity

Figure 5.10: The uniformly spaced array response for the UHF segment.

Looking at the UHF segment of the uniformly spaced array, the main lobe has a directivity of 23.53dB with a beamwidth of 3°. The largest side lobe occurs at 12.5° off the main lobe at a level of 1.41dB down from the main lobe. Additionally the back lobe has a directivity of 16.5dB down from the main lobe.

Continuing the same analysis with the VHF segment of the uniformly spaced array, as shown in Figure 5.11 below, the main lobe has a directivity of 22.71dB with a beamwidth of 8.8°. The largest sidelobe occurs at 47.5° off the main lobe at a level of 6.07dB down from the main lobe. Additionally, the back lobe has a directivity of 16.4dB down from the main lobe.
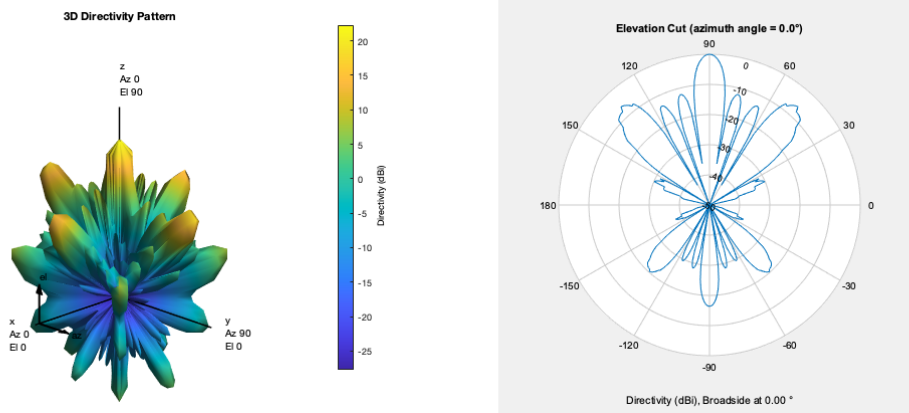
(a) Simulated 3D directivity pattern   (b) An elevation cut of the normalized directivity

Figure 5.11: The uniformly spaced array response for the VHF segment.

These results are presented in a tabular form in Table 5.3 below.

Geometry:	Pseudorandom		Uniform		Single Antenna	
Antenna Type:	UHF	VHF	UHF	VHF	UHF	VHF
Main Lobe Level (dB):	26.49	22.61	23.53	22.71	13.3	9.37
Side Lobe Suppression (dB):	11.43	13.9	1.41	6.05	14.8	-
Back Lobe Level (dB):	9.97	6.22	7	6.33	-3.36	-7.07
HPBW (rad):	0.04	0.11	0.05	0.16	0.84	1.01

Table 5.3: A comparison of the previously described pseudorandom arrangement, uniformly spaced array, and single antenna for both UHF and VHF segments of the proposed array. Here, side lobe suppression is defined as the difference in gain between the main lobe and the maximal sidelobe.

41

CHAPTER VI

FURTHER AND ONGOING RESEARCH

6.1 Other Pseudorandom Arrangements

In the pseudorandom arrangement used throughout this thesis, the coordinates were generated by using a random number generator which "chooses" from a uniformly distributed set of numbers. By changing tunable parameters in the code such as the distribution, the minimum element spacing, and the overall size of the array, particular array parameters can be achieved depending on what is desired. Based on those desired characteristics, large numbers of simulations can be ran until the optimal parameters have been found. For instance, if one wanted to simply maximize the power gain of the array, one could calculate that value for a particular geometry, slightly change the inter-element spacing, for example, and repeat this for a range of values until the maximum gain is found. Likewise, this can be done with different characteristics and different geometries. Methods to optimize hardware selection, array designs and implementations, and desired array characteristics will be followed up with in the future and can serve as a potential project with which to introduce students to simulation software and coding as well as understanding the basic operating principles of phased array technologies.

6.2 Potential Backend Systems

Another transceiver and data-taking implementation explored during this thesis involved utilizing Texas Instruments' AFE7920 wideband four-transmit four-receive IC in tandem with their JESD204B family of analog-to-digital converters (ADCs), high-speed digital-to-analog converters (DACs), and analog front ends (AFEs). The AFE7920 was to be be evaluated by utilizing the AFE7920EVM, an evaluation module equipped with 14-bit 12-GSPS digital-to-analog converters

(DACs), 14-bit 3-GSPS analog-to-digital converters (ADCs), and on-chip integrated PLL/VCO for high-frequency clock generation for DACs and ADCs.
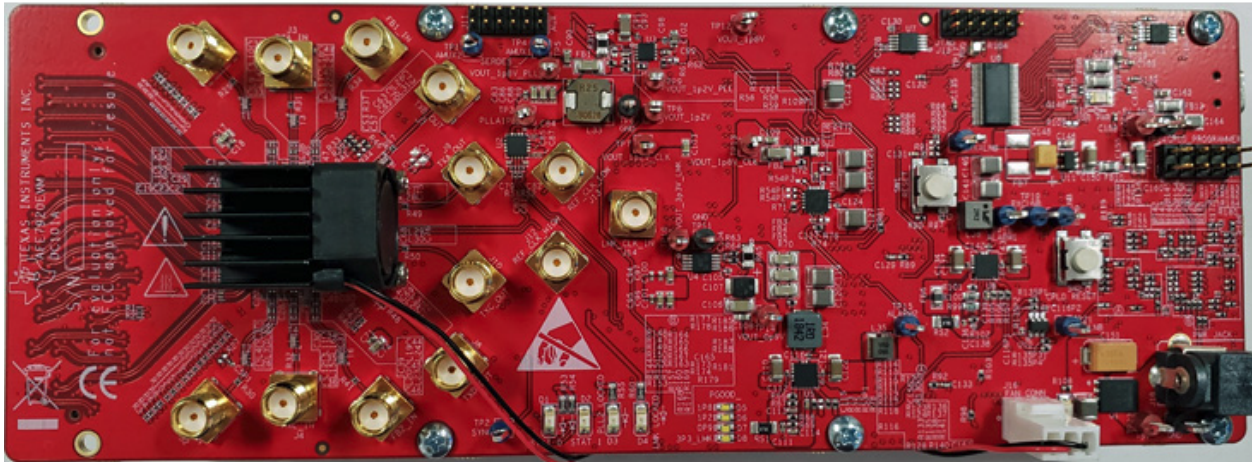
Figure 6.1: Texas Instruments' AFE7920 evaluation module [24].

Because this multi-channel transceiver module utilizes ADCs that sample up to 3 GSPS and DACs that sample up to 12GSPS, its maximum (without aliasing or undersampling) receive frequency is up to 1.5GHz and its maximum transmit frequency is up to 6GHz, covering many frequency bands utilized in satellite communications. The module also has a maximum receive bandwidth of 600MHz and a maximum transmit bandwidth of 1200MHz. The transceiver module interfaces with a data capture card via an onboard FMC connector. The TSW14J57EVM data capture card supports serial lanes speeds up to 15 Gbps and simply interfaces with a computer via a USB 3.0 cable. Together with the High-Speed Data Converter Pro (HSDC Pro) graphic user interface (GUI), it is a complete reconfigurable system that captures and evaluates data on each channel independently, making it an excellent solution for phased-array type applications.
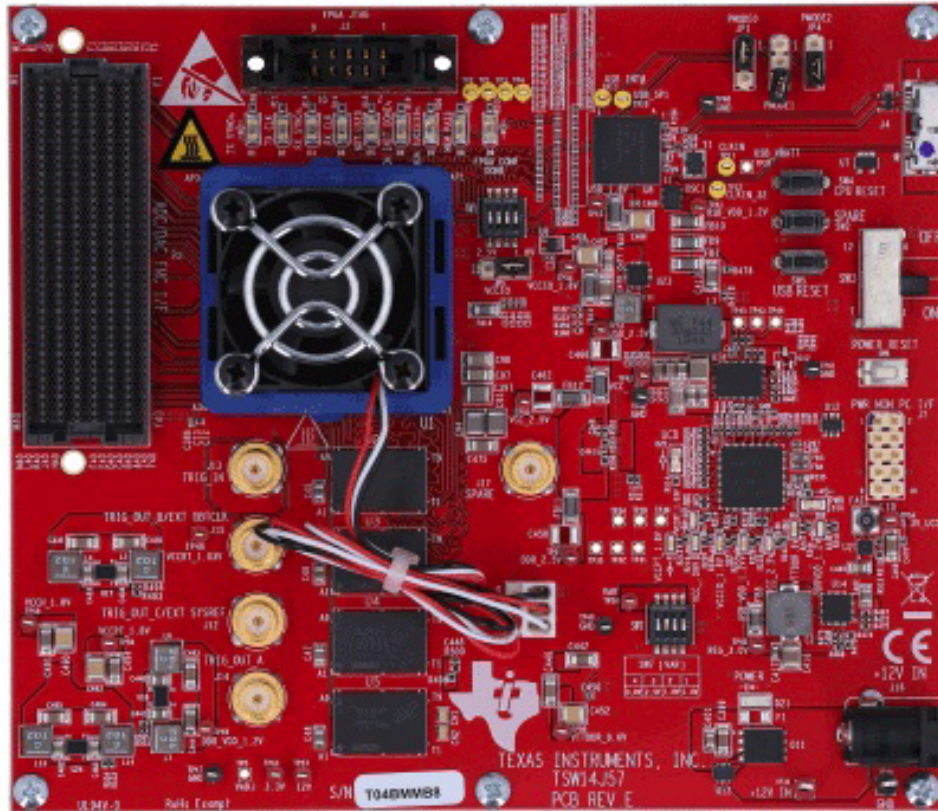
Figure 6.2: Texas Instruments' TSW14J57 data capture card evaluation module [25].

The transceiver evaluation module itself only supports up to 4 transmission and 4 receiving lines, however, if successfully demonstrated to be effective, as compared to purchasing a separate transceiver for each antenna, the transceiver chipset used in this evaluation model is attractive for making it a cost-efficient, scalable solution which would implement multiple chipsets on the same board for expanding the number of elements that data can be taken with in this array. Unfortunately, there were issues related to the initialization scripts required to fully demonstrate the capabilities of the transceiver evaluation module. This effort to demonstrate the capabilities of the Texas Instruments transceiver for application as a phased array backend including a demonstration of beamforming capabilities will continue to be explored as a viable option.

CHAPTER VII

CONCLUSIONS

We have shown that a pseudorandom arrangement of 20 antenna elements with a minimum inter-element spacing of 3 meters and a maximum array size of 16 meters in side length can provide higher gain when compared to that of a single antenna. In particular, we have shown a 13.9dB gain increase in the UHF band and a 13.24dB gain increase in the VHF band for the pseudorandom arrangement previously analyzed in this thesis. Additionally, that same pseudorandom arrangement provides a 2.96dB gain increase relative to a uniformly distributed array with an inter-element spacing of 3 meters in the UHF band and a similar gain with a difference of 0.1dB in the VHF band. The side lobes are also shown to be more significantly suppressed when using the pseudorandom arrangement as compared to the uniform array by 10.02dB more in the UHF band and 7.85dB more in the VHF band.

Ultimately, this array will serve to be a demonstration of a phased-array satellite ground station built using commercial-off-the-shelf (COTS) components and capable of communicating with and tracking spacecraft. Other potential applications include astrophysical observations of radio sources and asteroid/debris tracking. In addition, after the array has been built, it can serve as a developmental test bed in which new algorithms, transceiver systems, digital backends, antennas, and other components can be deployed modularly for research and development purposes.

BIBLIOGRAPHY

[1] ITU Radio Regulations, Section IV. Radio Stations and Systems – Article 1.63, definition: earth station

[2] Tzinis, Irene. "Visiting DSN Complexes." *NASA*, NASA, 30 Mar. 2020, `https://www.nasa.gov/directorates/heo/scan/services/networks/deep_space_network/complexes/visiting`

[3] International Astronomical Union 2011, *Cambridge.org*, `https://www.cambridge.org/core/services/aop-cambridge-core/content/view/S1743921311003565`

[4] "Appendix B". *History.nasa.gov*, `https://history.nasa.gov/SP-4217/app-b.htm`

[5] "The First Satellite Communications Engineers." The Communications Miracle: The Telecommunication Pioneers From Morse to the Information Superhighway, by John Bray, Plenum, 1995, pp. 250–251.

[6] "Telstar - Satellite Components." *National Air and Space Museum*, 22 Mar. 2017, `airandspace.si.edu/stories/objects/telstar-satellite-components.`

[7] The New Rockets Racing to Make Space Affordable, *Bloomberg.com*, `https://www.bloomberg.com/graphics/2018-rocket-cost/`

[8] Mazda, Xerxes; Mazda, F. F. (1999). *The Focal Illustrated Dictionary of Telecommunications*. Taylor & Francis. p. 476.

[9] "The Nobel Prize in Physics 1909." *NobelPrize.org*, `www.nobelprize.org/prizes/physics/1909/braun/biographical/`

[10] Nordrum, Amy; Clark, Kristen (January 27, 2017). "Everything You Need to Know About 5G". IEEE Spectrum Magazine. Institute of Electrical and Electronic Engineers. `https://spectrum.ieee.org/video/telecom/wireless/everything-you-need-to-know-about-5g`

[11] Phased Array Radar, *DARPA.mil*, `https://www.darpa.mil/about-us/timeline/phased-arrays`

[12] Cheng, Yao & Song, Nuan & Roemer, Florian & Haardt, Martin & Henniger, Hennes & Metzig, Robert & Diedrich, Erhard. (2012). Satellite Ground Stations with Electronic Beam Steering. 10.1109/ESTEL.2012.6400173.

[13] LINKS: Electronically Steered Array, (April 17, 2020) *ATLAS Space Operations*
`https://atlasground.com/links/`

[14] Henry, Caleb. (May 9, 2019) "Lockheed Martin Mulls Electronically Steered Antennas For Verge Ground Station Expansion." *SpaceNews*
`https://spacenews.com/lockheed-martin-mulls-electronically-steered-\`
`antennas-for-verge-ground-station-expansion/`

[15] IEEE Std 149-1979 (R2008), "IEEE Standard Test Procedures for Antennas". Reaffirmed December 10, 2008, Approved December 15, 1977, IEEE-SA Standards Board. Approved October 9, 2003, American National Standards Institute.

[16] IAU General Assembly Meeting, 1973, Commission 40 (Radio Astronomy/Radioastronomie), 8.

[17] Volakis, John Leonidas. *Antenna Engineering Handbook*. Fourth ed., McGraw Hill Education, 2007.

[18] Delos, Peter, et al. "Phased Array Antenna Patterns-Part 1: Linear Array Beam Characteristics and Array Factor." *Phased Array Antenna Patterns-Part 1: Linear Array Beam Characteristics and Array Factor | Analog Devices*, Analog Devices, May 2020,
`www.analog.com/en/analog-dialogue/articles/phased-array-antenna-patterns\`
`-part1.html.`

[19] LMR-400 Flexible Low Loss Communications Coax, *Times Microwave Systems*
`https://www.timesmicrowave.com/DataSheets/CableProducts/LMR-400.pdf`

[20] Advantages of Direct RF Sampling Architectures, (March 5, 2019) *National Instruments*
`https://www.ni.com/en-us/innovations/white-papers/18/`
`advantages-of-direct-rf-sampling-architectures.html`

[21] Kester, Walt. "What the Nyquist Criterion Means to Your Sampled Data System Design." *Analog Devices*.
`https://www.analog.com/media/en/training-seminars/tutorials/MT-002.pdf`

[22] ARISS: Contact the ISS, *ARISS.org*,
`https://www.ariss.org/contact-the-iss.html`

[23] "Antenna Array Factor Calculator." *Antenna Array Calculator*, 2013,
`antennaarraycalculator.blogspot.com/p/help.html.`

[24] "AFE7920EVM." *AFE7920EVM Evaluation Board | TI.com*,
`www.ti.com/tool/AFE7920EVM.`

[25] "TSW14J57EVM." *TSW14J57EVM Evaluation Board | TI.com*,
`www.ti.com/tool/TSW14J57EVM.`

APPENDIX A

APPENDIX A

PSEUDORANDOM ARRAY GEOMETRY CODE

The following code was written in Python to generate the coordinates for the antenna array.

```python
import numpy as np
coords = [ ] # This should become an n x 2 array where each row is
    the nth element's (x,y) coordinates
n = 20 # Number of elements in the array
radius = 3 # Minimum radius for each element to be spaced in meters
low_bound = -8 # A lower bound on the uniform distribution which
    determines the size of the array in meters
upper_bound = 8 # An upper bound on the uniform distribution which
    determines the size of the array in meters
# Create a random coordinate, a (2,1) array, that has a uniform
    distribution over [low_bound, upper_bound)
coord = np.random.uniform(low=low_bound, high=upper_bound, size=2)
coords.append(coord) # Add this first coordinate to the coords list
counter = 1 # Initialize a counter at 1 used to keep track of how
    many elements are in the list
loops = 0 # Initialize a loop counter to keep track of number of
    iterations looped over
while counter < n: # While the number of coordinates in the list is
    less than the required number of elements
    flag = True # Initialize a flag as True
    coord = np.random.uniform(low=low_bound, high=upper_bound, size
        =2) # Generate a new coordinate
    for i in range(counter): # Iterate through each element in the
        existing list and check the Euclidean distance
```

49

```python
            distance = np.sqrt( (coord[0] - coords[i][0])**2 + (coord[1]
                - coords[i][1])**2 )
            if distance < radius: # If distance < radius, Flag becomes
                false and generates a new coordinate.
                flag = False
                coord = coord = np.random.uniform(low=low_bound, high=
                    upper_bound, size=2)
                loops = loops + 1
                break
            if distance >= radius: # If distance >= radius, go on
                continue
        if flag == True: # Check the flag. If it's True, add it to the
            list. Loop again.
            counter = counter + 1
            coords.append(coord)
new_coords = np.zeros((n,2)) # Instead of a list of 1D Numpy arrays,
    create a large 2D Numpy array.
for i in range(len(coords)):
    new_coords[i] = coords[i] # new_coords is now the 2D array of
        antenna element coordinates
new_coords = np.zeros((n,2))
for i in range(len(coords)):
    new_coords[i] = coords[i]
print(new_coords) # Print the array of coordinates.
```

Listing A.1: The Python code written to generate the pseudorandom array antenna coordinates.

50

APPENDIX B

APPENDIX B

UHF ANTENNA SIMULATION MATLAB CODE

```
% This models the 436CP16 antenna.
% Parameter: Datasheet / Model
% Gain: 13.3dBic / 13.3dBi
% Front-to-back: 15dB / 16.6dB
% HPBW: 42.0 / 48.0


d1 = dipole('Length',12.625*.0254,'Width',cylinder2strip((3/32)
    *.0254),'Tilt',90,'TiltAxis',[0 1 0]);
d2 = dipole('Length',12.250*.0254,'Width',cylinder2strip((3/32)
    *.0254),'Tilt',90,'TiltAxis',[0 1 0]);
d3 = dipole('Length',11.937*.0254,'Width',cylinder2strip((3/32)
    *.0254),'Tilt',90,'TiltAxis',[0 1 0]);
d4 = dipole('Length',11.750*.0254,'Width',cylinder2strip((3/32)
    *.0254),'Tilt',90,'TiltAxis',[0 1 0]);
d5 = dipole('Length',11.531*.0254,'Width',cylinder2strip((3/32)
    *.0254),'Tilt',90,'TiltAxis',[0 1 0]);
d6 = dipole('Length',11.375*.0254,'Width',cylinder2strip((3/32)
    *.0254),'Tilt',90,'TiltAxis',[0 1 0]);
r = dipole('Length',13.687*.0254,'Width',cylinder2strip((3/32)*.0254)
    ,'Tilt',90,'TiltAxis',[0 1 0]);

uhf = quadCustom(...
    'Exciter',dipole('Length',13.625*.0254,'Width',cylinder2strip
        ((3/32)*.0254),'Tilt',90,'TiltAxis',[0 1 0]),...
    'Director', {d1 d2 d3 d4 d5 d6},...
```

```matlab
      'DirectorSpacing', [(17-14.562) (23.313-17) (31.875-23.313)
         (41.813-31.875) (51.563-41.813) (61-51.563)]*.0254,...
      'Reflector',{r},...
20    'ReflectorSpacing', 2.562*.0254,..
      'BoomLength', 65.75*.0254,...
      'BoomWidth', cylinder2strip((1/2)*.0254),...
      'BoomOffset',[0 0.005 (((65.75)/2)-14.562)*.0254],...
      'Tilt',90,...
25    'TiltAxis',[0 1 0]);


figure
pattern(uhf,436e6)


30 figure
patternAzimuth(uhf,436e6);


figure
show(uhf)
```

Listing B.1: The code written in MATLAB to simulate an individual UHF antenna.

APPENDIX C

APPENDIX C

ARRAY SIMULATION MATLAB CODE

```matlab
fc =435e6; % For UHF = 435e6, for VHF = 146e6
c = physconst('LightSpeed');
ant = uhf;
wavelength = c/fc;


% Create an arbitrary array which takes in custom coordinates.
arbitrary = phased.ConformalArray(...
    'ElementPosition', [-4.29842954311602 2.3546283467097275
        -7.912256000697484 6.438089637760736 4.5776928224254405
        0.6114083762343334 4.3491466713765625 -6.978679013358557
        6.964229482301359 -2.638378749849286 3.8559250832060386
        -2.5572254930149825 -1.3326465838541584 -6.266881989810605
        0.6070051482277137 -7.4675031752086 0.40120979820752467
        7.536624862621524 3.053825753918666 -1.3515337413772084 ;
        -6.4414991413467675 -7.7981345390623655 -6.290064521443938
        7.702090051841351 -3.7192665716494435 -1.25566398435347
        0.1276082372219225 2.252177479694957 3.2949516453081067
        4.215300908212189 4.157452247154753 -2.728518947281204
        6.989500794141902 -1.4034674523616246 -4.972862289530184
        7.85681577520325 4.181478934647917 -1.3631776200798864
        7.921167173856714 1.4380251430317603 ; 0 0 0 0 0 0 0 0 0 0 0 0 0
         0 0 0 0 0 0 0 ],...
    'ElementNormal', [0;90],...
    'Element',ant);
```

```matlab
% This is a uniformly spaced (5x4) array with 3m spacing between each
% antenna. Uncomment to analyze.
%arbitrary = phased.ConformalArray(...
%     'ElementPosition', [0 3 6 9 0 3 6 9 0 3 6 9 0 3 6 9 0 3 6 9;...
%      0 0 0 0 3 3 3 3 6 6 6 6 9 9 9 9 12 12 12 12;...
%      0 0 0 0 0 0 0 0 0 0 0 0 0 0 0 0 0 0 0 0],...
%     'ElementNormal', [0;90],...
%     'Element',ant);

% View the array elements by uncommenting below.
%figure
%viewArray(arbitrary,'showNormals',true,'ShowIndex','All')

% Look at the overall array's beam pattern.
figure
pattern(arbitrary,fc);

% Show an azimuthal cut of the array's beam pattern.
figure
patternAzimuth(arbitrary,fc)

% Show an elevation cut of the array's beam pattern.
figure
patternElevation(arbitrary,fc,'Elevation',-90:0.01:90);
```

Listing C.1: The code written in MATLAB to simulate the pseudorandom arrangement analyzed in the thesis. This can be used and generalized to any arbitrary geometry.

BIOGRAPHICAL SKETCH

Brent K. Cole currently works at The University of Texas Rio Grande Valley (UTRGV) within the Center for Advanced Radio Astronomy (CARA) as the laboratory coordinator and lead technician for the Spacecraft Tracking and Research into Gigahertz Astrophysical Transient Emission (STARGATE) laboratory where he manages electronics, radio-frequency (RF) instrumentation and general upkeep of the lab, has mentored and given tours to students, and performed electronics diagnostics and repairs for projects as needed. He earned his Bachelor of Science in Physics at the University of Texas at Austin (UT) in 2017 and earned his Master of Science in Physics from UTRGV in December 2020.

Over the course of his education, he has worked as part of many collaborative teams with both academic and commercial interests. As part of UTRGV's Low Frequency All Sky Monitor (LoFASM) team, he has traveled to the National Radio Astronomy Observatory (NRAO), NASA's Goldstone Deep Space Communications Complex, and Hillsdale College to work on radio telescope instrumentation and hardware, including the design and development of a system to enable remotely controlling data-taking modes. As part of SG1, a handpicked student group within CARA geared towards developing new technologies that solve industry problems, he collaborated with an S&P 500 company to test and develop the hardware for a remote sensing application.

In addition to his academic career, Brent is also a highly-driven entrepreneur and a co-founder of a technology startup company based in Brownsville, Texas where he oversees the commercial hardware development. He can be reached at brentkcole@gmail.com.